JG|U

Johannes Gutenberg University Mainz
FB08
Institute of Physics

Master Thesis

Reconstruction and Background Discrimination in a Hybrid and Opaque Scintillator Detector

Kyra Mossel

1. Reviewer   Prof. Dr. Sebastian Böser
Institute of Physics
Johannes Gutenberg University Mainz

2. Reviewer   Prof. Dr. Michael Wurm
Institute of Physics
Johannes Gutenberg University Mainz

June 24, 2024

Kyra Mossel

Reconstruction and Background Discrimination in a Hybrid and Opaque Scintillator Detector

Master Thesis, June 24, 2024

Reviewers: Prof. Dr. Sebastian Böser and Prof. Dr. Michael Wurm

Johannes Gutenberg University Mainz

AG Böser

Institute of Physics

Faculty of Physics, Mathematics and Computer Science

Staudingerweg 7

55128 Mainz

Abstract

This thesis presents a comprehensive study of the event reconstruction for the NuDoubt^{++} experiment, a novel experiment aimed at measuring neutrinoless double beta decay. The detector leverages advanced scintillator technologies—opaque and hybrid scintillators—to achieve low background interference and high energy resolution. The design features a cylindrical tank filled with a scintillator, intersected by a dense grid of wavelength-shifting fibers for effective scintillation light readout.

A simulation of the opaque scintillator part of the detector as well as a reconstruction is developed. It is investigated how different arrangements of the fibers influence the performance. With the developed reconstruction positional resolution better than 1 mm is achieved. For the photon number resolution, 4 % at photon numbers corresponding to a particle energy of 1 MeV is reached. Additionally, the background discrimination potential using the hybrid scintillator is analyzed. There, it is taken advantage of the fact, that different particles create different ratios of Cherenkov and scintillation light. This can be used to identify particle events and discriminate background especially relevant for the search of the rare neutrinoless double beta decay. High discrimination potential for double positron decay modes has been found, demonstrating the potential of the NuDoubt^{++} experiment.

Contents

Introduction

Neutrinos, electrical neutral particles with tiny masses, play a fundamental role in the Standard Model of particle physics and our understanding of the universe. Though they have a high abundance, neutrinos are extremely challenging to detect due to their rare interactions with matter. Their elusive nature has driven extensive research aimed at uncovering their properties. One of the most intriguing phenomena in neutrino physics is the search for neutrinoless double beta decay. If this hypothetical process is observed, it would have profound implications for our understanding of particle physics. It would not only confirm the Majorana nature of neutrinos — suggesting that neutrinos are their own antiparticles — but also provide insights into the absolute scale of neutrino masses [1]. The discovery of neutrinoless double beta decay would significantly enhance our understanding of lepton number conservation and provide important clues about the matter-antimatter asymmetry in the universe.

Limits on the order of 10^{26} years for the lower half-life of neutrinoless double beta minus decays has been achieved for several isotopes by Current double beta decay experiments [2–4]. However, to probe the effective Majorana neutrino mass scale these limits need to be extended by several orders of magnitude. The NuDoubt^{++} experiment aims to explore the less investigated double beta plus decay modes, which are expected to have even longer half-lives due to their lower available kinetic energy and the repulsive Coulomb force between positrons and the nucleus. Additionally, NuDoubt^{++} aims to achieve a measurement of the two-neutrino mode of double beta plus decay involving positron emission, a process predicted by the Standard Model but not yet observed. This decay mode, which involves the emission of two neutrinos alongside the beta plus decay, would provide valuable confirmation of neutrino properties and interactions. Successfully detecting this decay mode would validate current models and provide a deeper understanding of the fundamental symmetries and conservation laws in particle physics.

NuDoubt^{++} is set to combine two novel liquid scintillator technologies: opaque scintillators, which can provide sub-centimeter-scale event topology information, and hybrid scintillators, which allow for the measurement of the ratio between

Cherenkov and scintillation signals. This dual approach enhances background discrimination capabilities compared to traditional organic scintillators and facilitates heavy isotope loading with minimal impact on scintillation output and energy resolution. For effective light collection, optimized wavelength-shifting fibers (OWL-fibers) are deployed in the detector.

This thesis concentrates on the event reconstruction of position and energy within the NuDoubt^{++} detector and examines the influence of various scintillator and detector design properties on the reconstruction performance. To achieve this, a simplified detector simulation has been developed. Additionally, this thesis focuses on background discrimination strategies using the hybrid scintillator.

An overview of current knowledge about neutrinos is provided in the next chapter (Chapter 2), along with a detailed discussion on double beta decay, followed by a brief section on event reconstruction methods. The NuDoubt^{++} experiment is then described in Chapter 3, with emphasis on the opaque and hybrid scintillator technologies. A theoretical mode based on random walk is introduced in Chapter 4, followed by results on reconstruction performance for various detector configurations. Subsequently, the strategy for background discrimination based on the ratio of Cherenkov and scintillation light is discussed Chapter 5, with discrimination factors obtained from simulations.

Theory 2

This chapter offers a concise overview of the historical trajectory of neutrino physics. Additionally, neutrinoless double beta decay is presented in Section 2.2, an elusive process yet to be observed. Furthermore, event reconstruction is discussed in Section 2.3, providing insights into the data analysis technique used later on.

2.1 Neutrino history

The existence of neutrinos was first postulated by Wolfgang Pauli in 1931 to account for the continuous spectrum observed for the electrons emitted during β-decays [5]. In a hypothetical scenario where only two particles - electron and proton - are the product of a β-decay, the emitted electron would possess only a discrete energy due to the conservation laws of energy, momentum, and spin. The observation of a continuous spectrum led to the prediction of a third, uncharged particle, which is known as the neutrino today. Enrico Fermi developed the first theory incorporating neutrinos into β-decay processes in 1933 [6]. Experimental confirmation of the electron anti-neutrino's existence came in 1956 through the work of F. Reines and C. L. Cowan, who utilized the flux from a nuclear reactor [7]. Subsequent experiments conducted by L. Lederman, M. Schwartz, and J. Steinberger in 1962 at the Alternating Gradient Synchrotron located at the Brookhaven National Lab confirmed the existence of another type of neutrino, the muon neutrino [8]. This discovery established the presence of two distinct types of neutrinos, each interacting separately with their corresponding charged leptons. In 1989, measurements of the width of the Z^0 resonance by experiments at the Large Electron-Positron Collider (LEP) established that the total number of neutrino flavors participating in weak interactions, with masses $\lesssim 45.6\,\text{GeV}$ (half the mass of the Z^0 boson), was three [9–11]. However, this does not preclude the existence of additional sterile neutrinos, which do not participate in weak interactions. Finally, the tau-neutrino, the third neutrino type, was detected by the DONUT experiment in 2000 [12].

Standard Model of Elementary Particles
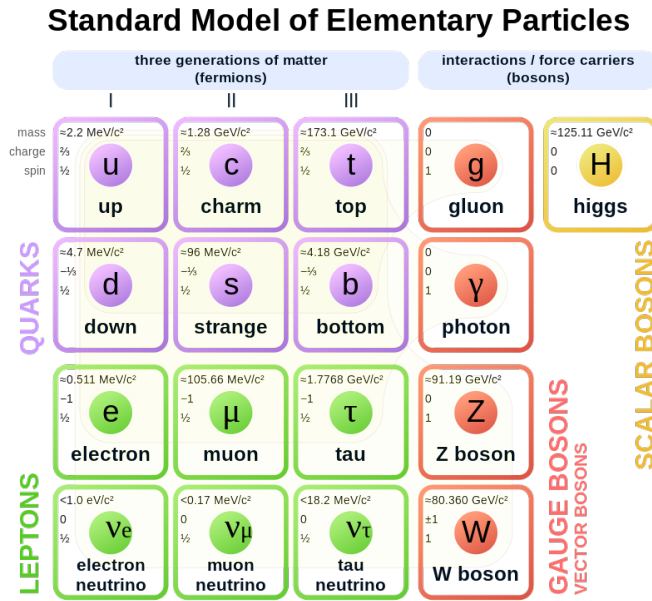
Fig. 2.1: The Standard Model of elementary particles [13].

Neutrinos belong to the lepton family of particles in the Standard Model (SM) of particle Physics (see Figure 2.1). As leptons, they are fermions with a spin of $\frac{1}{2}$. Additionally, neutrinos have no charge and thus only interact weakly. Inside the Standard Model, neutrinos are assumed to be massless. This assumption has been disproved by the discovery of neutrinos oscillations. Neutrinos exhibit flavor oscillations, a phenomenon in which they switch between different flavor states as they propagate through space. The concept of neutrino oscillations was proposed by B. Pontecorvo in 1957 [14, 15], with the formalism of mixing between mass and flavor eigenstates introduced by Z. Maki, M. Nakagawa, and S. Sakata in 1962 [16]. The mixing between the different states is described with the PMNS matrix, which contains the mixing angles θ_{ij} between the states and a single phase angle called δ_{CP} related to charge-parity violations. Experimental evidence for neutrino oscillations emerged from solar and atmospheric neutrino experiments. The Homestake experiment [17] in 1968, led by R. Davis, measured solar neutrinos for the first time, revealing a flux significantly lower than predicted by the standard solar model [18]. The discrepancy was confirmed by different experiments afterwards [19–22]. Similar anomalies were observed in atmospheric neutrinos by experiments such as Kamiokande and MARCO starting in the 1980s [23–26]. The Super-Kamiokande experiment provided clear evidence of neutrino oscillations in atmospheric neutrinos in 1997 [27]. Neutrino oscillations have been

extensively studied in various experiments, leading to precise measurements of mixing angles and mass squared differences $\Delta m_{ij}^2 = m_i^2 - m_j^2$. The sign of Δm_{21}^2 is known to be positive, while the sign of Δm_{31}^2 is not yet established, leaving open two possibilities, normal ordering (NO) or inverted ordering (IO) [28]. The first hints of CP violation have been reported: there is a preference for large CP violation, although CP conservation is still allowed at 3σ for NO. The discovery of neutrino oscillations established that neutrinos possess mass, challenging the assumption of mass-less neutrinos in the Standard Model. To this day, the neutrino mass remains unknown, with only upper limits established [29].

In 1937, E. Majorana proposed the Majorana nature of neutrinos, suggesting that neutrinos could be their own antiparticles. Unlike charged fermions, which are typically Dirac particles and carry U(1) quantum numbers such as electric charge, Majorana fermions do not carry these quantum numbers. If neutrinos are Majorana particles, this could lead to violations of lepton number conservation. The distinction between Majorana and Dirac neutrinos is crucial for understanding fundamental symmetries in nature. Neutrino oscillations do not distinguish between Majorana and Dirac particles, as they do not inherently violate lepton number conservation. To determine whether neutrinos are Majorana or Dirac particles, a process is needed that allows for lepton number violation. The most sensitive process is neutrinoless double-beta ($0\nu\beta\beta$) decay, which experimentally tests lepton number violation and if neutrinos are Majorana particles.

2.2 Double beta decay

Double beta decay ($\beta\beta$) is a rare nuclear process wherein the nucleus undergoes a transformation, changing its charge Z by two units while the total number of nucleons A is conserved. It was first introduced by M. Goeppert-Mayer in 1935 [30]. Double beta decay can be the only observable decay mode for certain isotopes, where single β transitions are energetically suppressed or forbidden. Because of the nuclear pairing interaction, nuclei with even numbers of protons and neutrons are more stable than those with odd numbers. Consequently, even-even nuclei can be more tightly bound than their odd-odd counterparts, in which they would decay with a single β transition, but decays into a less bound isotope are energetically suppressed. These nuclei then can decay via double beta decay into the next even-even nuclei, which are more strongly bound (see Figure 2.2). Alternatively,
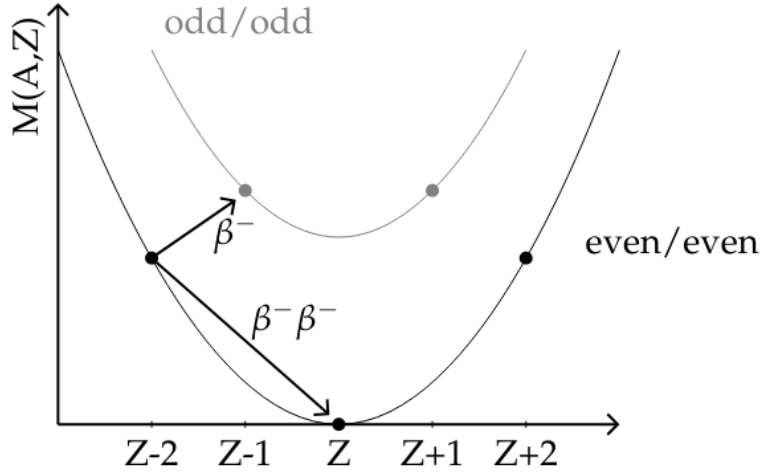
Fig. 2.2: Mass parabolas of nuclear isobars with even A. Due to the attractive nuclear pairing interaction, single beta transitions (β) of even-even nuclei to their odd-odd isobaric neighbor can be energetically forbidden, whereas in a second-order process, double beta decay ($\beta\beta$) is allowed [32].

single beta decays may be suppressed due to significant disparities in total angular momentum between the initial and final nuclei, resulting in comparable rates for single beta and double beta transitions [31].

Double beta decay occurs via weak interaction and is characterized by exceptionally long half-lives due to its second-order nature. There are two distinct types of double beta decays: the SM two neutrino decay (2ν), in which two neutrinos or antineutrinos are emitted in the final state, and the neutrinoless decay (0ν), where no neutrinos are emitted.

Double beta decay can occur in various modes, including $\beta^-\beta^-$, $\beta^+\beta^+$, electron capture with positron emission ($\mathrm{EC}\beta^+$) and double electron capture (ECEC). The corresponding decay expressions for the 2ν-mode are outlined in equations (2.1) to (2.4).

$$2\nu\beta^-\beta^- : (A, Z) \rightarrow (A, Z + 2) + 2e^- + 2\overline{\nu} \tag{2.1}$$

$$2\nu\beta^+\beta^+ : (A, Z) \rightarrow (A, Z - 2) + 2e^+ + 2\nu \tag{2.2}$$

$$2\nu\mathrm{EC}\beta^+ : (A, Z) + e^- \rightarrow (A, Z - 2) + e^+ + 2\nu \tag{2.3}$$

$$2\nu\mathrm{ECEC} : (A, Z) + 2e^- \rightarrow (A, Z - 2) + 2\nu \ . \tag{2.4}$$

As an example, the Feynman diagram of $2\nu\beta^-\beta^-$ is shown in Figure 2.3a. These

(a) $2\nu\beta^-\beta^-$

(b) $0\nu\beta^-\beta^-$
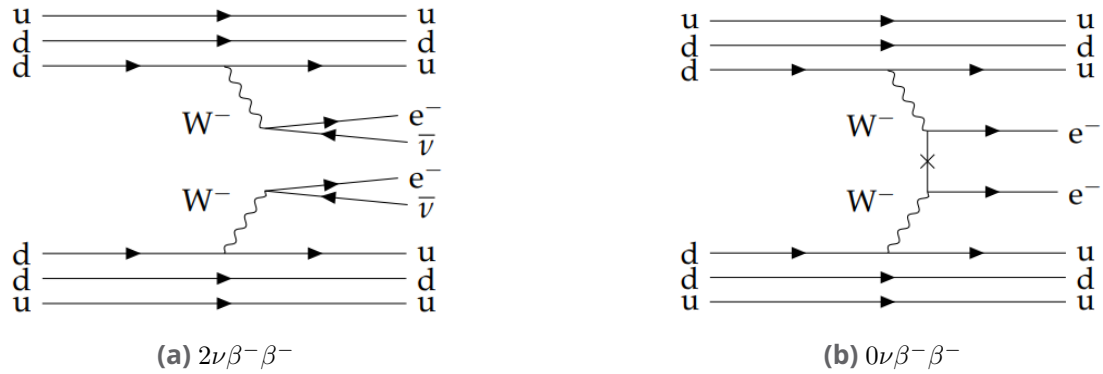
Fig. 2.3: Feynman diagrams of the (a) SM $2\nu\beta^-\beta^-$ decay and (b) the lepton number non-conserving $0\nu\beta^-\beta^-$ decay in the light-neutrino exchange scenario.

decays can also occur in a neutrinoless mode (0ν), where no neutrinos are emitted. For example, the expression for neutrinoless for neutrinoless double beta minus decay is:

$$0\nu\beta^-\beta^- : (A, Z) \rightarrow (A, Z + 2) + 2e^-. \tag{2.5}$$

In $0\nu\beta\beta$ decay the final state is composed of the nuclear recoil and the two electrons or positrons. In case of $\beta^+\beta^+$ the two positrons will annihilate emitting two pairs of 511 keV gamma rays, which is a valuable signature for experiments. Because the electron mass is significantly smaller than that of the daughter nucleus - by several orders of magnitude - the energy transferred to the nucleus during the decay is negligible, resulting in minimal nuclear recoil. Thus, the sum of the electron (or positron) energies is practically equivalent to the Q-value $Q_{\beta\beta}$ of the decay.

In the two-neutrino decay, the final state includes the nuclear recoil, two electrons (or positrons) and two antineutrinos (or neutrinos). Because neutrinos have a very low interaction cross-section, they escape undetected. Hence, the sum of the energy of the leptons (electrons or positrons) in this process is less than or equal to the Q-value of the double beta decay, resulting in a continuous energy spectrum from 0 to $Q_{\beta\beta}$. In contrast, for the neutrinoless decay mode the total energy of the emitted leptons should be approximately equal to the Q-value, forming a distinct peak at $Q_{\beta\beta}$, as shown in 2.4. This peak allows for potential detection of neutrinoless double beta decay, provided the experimental setup has sufficiently good energy resolution to accurately detect and resolve this peak.

The two neutrino decay modes are well-described by the Standard Model and $2\nu\beta^-\beta^-$ has been experimentally observed in several isotopes, typically with half-lives on the order of 10^{19} to 10^{21} years [33]. The decay modes characterized by
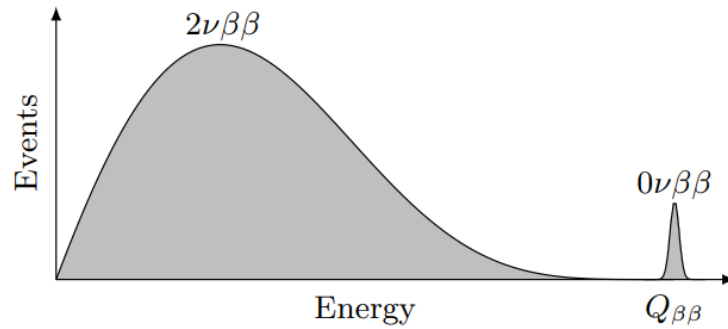
Fig. 2.4: Theoretical spectra of $2\nu\beta\beta$ and $0\nu\beta\beta$ decays with 1.5 % energy resolution (FWHM). The relative normalization is for illustrative purpose only [32].

decreasing charge exhibit significantly longer half-lives due to the reduced kinetic energy available. Additionally, in positron-emitting modes, the half-lives are prolonged by the Coulomb repulsion experienced by positrons from the nucleus. Notably, among these decay modes, only the 2νECEC decay has been experimentally confirmed in isotopes such as ^{130}Ba [34], ^{78}Kr [35] and ^{124}Xe [3]. The limited exploration of these modes arises from smaller phase space factors leading to suppressed decay probabilities, less favorable decay Q-values, and low natural abundances of suitable candidate nuclei [36].

However, neutrinoless double beta decay modes have yet to be observed. These modes, violating total lepton number conservation, would signify the Majorana nature of neutrinos and provide crucial insights into physics beyond the Standard Model [37]. In the simplest and most studied case, in which massive neutrinos are added to the SM and assumed to be Majorana particles, the $0\nu\beta\beta$ decay can happen via the exchange of a light Majorana neutrino. This is the so-called light-neutrino exchange scenario. The Feynman diagram for the $0\nu\beta^-\beta^-$ decay in the light-neutrino exchange scenario is shown in Figure 2.3b. In addition, several other theoretical models have been proposed to explain potential mechanisms for neutrinoless double beta decay [32].

The half-lives of neutrinoless double beta decay modes are anticipated to be significantly longer, typically ranging from 3 to 5 orders of magnitude higher than those of the corresponding two-neutrino decay modes. Conversely, decay modes involving positron emission are expected to exhibit an even larger half-life compared to the $0\nu\beta^-\beta^-$ mode. The rate of neutrinoless double electron capture (0νECEC) may be notably enhanced due to resonance effects [38–40]. This decay

is therefore considered to have great potential for the discovery of the Majorana mass of neutrinos.

2.3 Parameter reconstruction

In particle experiments, measurements $\vec{x}$ are obtained from the detector system. From these measurements the properties of the underlying physical events need to be inferred. To accomplish this, the properties of the event has to be described by a model using a set of parameters θ. This model should describe how the parameters θ relate to the observed data x. For instance, a parameter might represent the spatial coordinates of a particle's interaction within the detector or the energy of the particle.

The goal of reconstruction or parameter estimation is to determine the most likely values for the parameters θ given the measurement x.

2.3.1 Maximum likelihood estimation

One common approach for this purpose is the maximum likelihood estimation (MLE). The basic idea of the concept goes back to Ronald Fisher [41, 42]. In MLE, a likelihood function is constructed to quantify how likely the observation of data x for different values of the parameters θ is. This likelihood function $L(\theta|x)$ establishes the connection between the observed data and the model parameters via probability distributions. Assuming that $p(x|\theta)$ is the probability density function (PDF) for observing a specific value of x given θ, the likelihood for a measurement x_1 is then $L(\theta|x_1) = p(x_1|\theta)$. For N measurements $\vec{x} = (x_1, x_2, ..., x_N)$ the likelihood is calculated by the product of the individual probabilities

$$L(\theta|\vec{x}) = \prod_{i=1}^{N} p(x_i|\theta). \tag{2.6}$$

To find the optimal values of the model parameters θ_{opt}, $L(\theta|\vec{x})$ has to be maximized with respect to θ. Unlike $p(x|\theta)$, the likelihood $L(\theta|\vec{x})$ is no longer a PDF since it is not normalized. As the values of L are usually very small, it is common to use the logarithm of the likelihood $\mathcal{L} = \ln(L)$ to ensure numerical stability. The

log-likelihood is sometimes denoted as LLH. Additionally, instead of maximizing $\mathcal{L}$ minimizing -$\mathcal{L}$ can be preferred.

The fundamental principle behind maximum likelihood estimation is that the correct likelihood function contains all the information which can be extracted from the measurement data [43]. This means that if the likelihood function is correctly specified, it effectively captures all relevant information for parameter estimation. Accordingly, maximizing this function with respect to the parameters θ yields the best-fit values that maximize the probability of observing the given data. It is important to note that the parameters obtained through MLE are the most probable given the information provided by the detector, but they do most of the times not correspond to the true parameters characterizing the underlying physical event.

2.3.2 Chi-squared minimization

In addition to Maximum Likelihood Estimation (MLE), another widely used approach for parameter estimation is fitting a model to data by minimizing the sum of squared differences between the observed data and the model predictions. When fitting a model to data, the goal is to determine the set of parameters θ that best describe the relationship between the observed measurements $\vec{x}$ and the underlying model. Suppose we have a model function $f(x|\theta)$ that predicts the expected value of the observations based on the parameters. The task is then to find the parameters θ that minimize the difference between the observed data x_i^{obs} and the model predictions x_i^{pred}.

If the uncertainties of the predictions are denoted by σ_i for each measurement, the chi-squared χ^2 for N measurements is defined as:

$$\chi^2(\theta) = \sum_{i=1}^{N} \left(\frac{x_i^{\mathrm{obs}} - x_i^{\mathrm{pred}}(\theta)}{\sigma_i} \right)^2 . \tag{2.7}$$

Minimizing the chi-squared value with respect to θ yields the best-fit parameters, θ_{opt}, that minimize the discrepancy between the observed data and the model predictions, taking into account the uncertainty of the predictions.

The goodness of fit can also be assessed using the reduced chi-squared (χ^2_{red}), which is the chi-squared divided by the degrees of freedom (DoF). The degrees of freedom

are given by the number of data points N minus the number of fitted parameters p:

$$\chi^2_{\text{red}} = \frac{\chi^2(\theta)}{N - p} .$$

(2.8)

A reduced chi-squared value close to 1 indicates a good fit, whereas values significantly greater than 1 or much less than 1 suggest that the model may not be a good fit to the data or that the uncertainties have been incorrectly estimated.

NuDoubt^{++}

NuDoubt^{++} is a new experiment designed to explore the double beta decay modes including positron emission ($2\nu\beta^+\beta^+$, $2\nu\beta^+$EC, $0\nu\beta^+\beta^+$ and $0\nu\beta^+EC$) [44]. The detector will use the novel hybrid and opaque scintillator technologies, aiming to achieve a high sensitivity in the measurement of neutrinoless double beta decay processes.

The detector technology is explained with a focus on the hybrid and opaque scintillator technology in Section 3.1 as well as a short section about the OWL-fibers (Section 3.2). The planned detector design is presented in Section 3.3, followed by a discussion about the double beta isotopes suitable for the experiment. Section 3.5 gives a short overview of the background sources relevant in the search for double beta decay.

3.1 Liquid scintillator

It is distinguished between two kinds of scintillators: organic and inorganic scintillators. The scintillation process in inorganic materials is due to the electronic band structure found in crystals and is not molecular in nature as is the case with organic scintillators. Liquid scintillators are a special case of organic scintillators, where the scintillating material is dissolved in an organic solvent. The main objective of a scintillator is the conversion of the kinetic energy of an incoming particle into detectable light. The scintillation light is caused by the ionization of the scintillator molecules by the incident particle. This happens directly for charged particles as electrons or muons or indirectly for neutrinos, gammas or neutrons. In this case, the incoming particle transfers energy to the charged particles inside the scintillator, which then ionize the scintillator molecules. As the excited electrons return to their ground state (de-excitation), they release the excess energy in the form of photons.

In a scintillator molecule, each electronic energy state consists of multiple vibrational sub-states, which have much smaller energy differences compared to the electronic states. Excitation typically occurs from the vibrational ground state of the electronic ground state to an excited vibrational state of an excited electronic state. Vibrational states de-excite non-radiatively on a very short time scale, around 10^{-12} s, which is much faster than the de-excitation of the electronic states. The time scale for electronic de-excitation depends on whether the excited electronic state is a singlet (spin quantum number of zero) or a triplet (spin quantum number of one). For singlet states, typical decay times range from a few to tens of nanoseconds (fluorescence). For triplet states, decay times are much longer, often milliseconds or more (phosphorescence), due to the involvement of two excited molecules in the triplet annihilation reaction [45]. The decay of excited electronic states in a scintillator can be modeled by two (or more) exponential decay components:

$$N(t) = A_p \exp\left(-\frac{t}{\tau_p}\right) + A_d \exp\left(-\frac{t}{\tau_d}\right). \tag{3.1}$$

Here, τ_f and τ_s are the time constants for the prompt and delayed decay components, respectively. A_p and A_d represent the relative contributions of these components. t denotes time, and $N(t)$ is the number of photons produced as a function of time. The time constants for these processes are usually on the order of a few nanoseconds [46, 47]. Additional exponential decay components may be included to account for triplet states. Organic scintillators generally exhibit faster decay times compared to inorganic scintillators, which typically have decay times around 100 nanoseconds [48].

The light yield of a scintillator describes the number of scintillation photons produced based on the incident energy. Ideally, the energy emitted as scintillation light is proportional to the particle energy. Typically, between 3 % to 12 % of the energy is converted to scintillation light leading to a light yield of approximately 10^4 photons per MeV. However, in a more realistic scenario, particle- and energy-dependent losses of scintillation light occur, resulting in a non-linear relationship between the incoming energy and the scintillation light. The primary cause of this non-linearity is ionization quenching. This occurs because the density of ionized and excited molecules is high, leading to significant interactions between them. Quenching is more pronounced when the energy loss per unit path length $d\mathrm{E}/dx$ is large, such as at low energies towards the end of a particle track. Furthermore, the quenching effect is stronger for heavy particles. Birks' law provides an empirical

equation to describe the light yield per unit path length as a function of the energy loss per unit path length, accounting for ionization quenching [49]:

$$\frac{d\mathrm{L}}{dx} = \mathrm{S}\frac{\frac{d\mathrm{E}}{dx}}{1 + k_B \frac{d\mathrm{E}}{dx}} \, .$$

(3.2)

Here, $d\mathrm{L}$ is the light produced by a particle along a path of length dx, S is the light yield constant, and k_B is Birks' quenching factor. For electrons, typical values are around 0.01 to 0.03 cm/MeV [50].

Liquid organic scintillators are made of one or more solvents, a fluor as solute and in most cases a wavelength shifter. When there is only one solvent, a major part of the fluorescent radiation is self-absorbed because the emission and absorption spectra overlap in a wide range. To prevent self-absorption, fluors are added. The absorption spectrum of the fluor shows a significant overlap with the emission spectrum of the solvent. So in total the emission spectrum is shifted to higher wavelengths. Ideally, the shift allows a more transparent region of the scintillator to be reached. Wavelength shifters are sometimes added to match the spectral sensitivity range of a readout device, e.g. a PMT. A wavelength shifter absorbs photons of a certain wave length and re-emits them at a larger wavelength.

Liquid scintillators are particularly suited for the detection of low-energy neutrinos due to its low energy threshold and high light yield, which leads to a good energy resolution. Other advantages are a high radio purity and its ability to cover large volumes at reasonable costs [45]. In recent years, novel ideas in the field of liquid scintillator technology emerged – most prominently opaque and hybrid scintillators – which add unprecedented particle discrimination power at MeV-scale to the list of their advantages [51].

3.1.1 Opaque scintillator

Opaque scintillators represent a novel advancement in scintillator technology, offering advantages over traditional transparent liquid scintillators. By incorporating additives like wax into transparent scintillator materials, opaque scintillators achieve comparable high light yields while introducing benefits in spatial resolution, absorption properties and particle identification capabilities [52].

The characteristic of an opaque scintillator is the short scattering length, typically in the order of a few millimeters, which effectively confines scintillation light

(a) Electron   **(b)** Gamma   **(c)** Positron
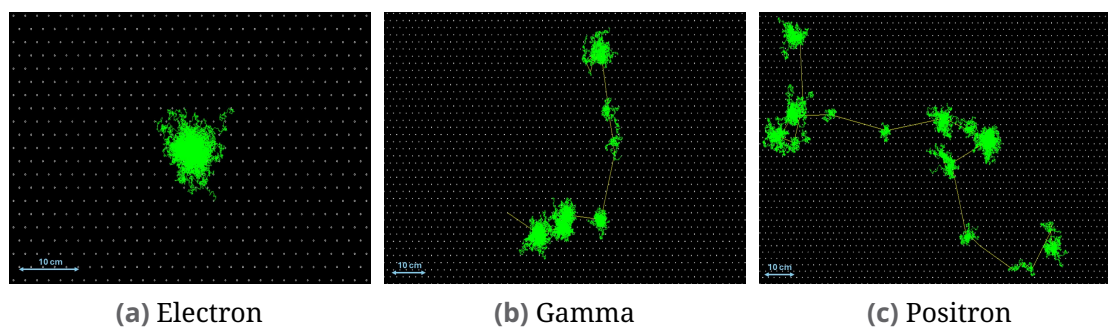
Fig. 3.1: Simulation of the pattern of different particles in an opaque scintillator equipped with optical fibers. The illustration is shown in the x-y-plane, with the fibers aligned parallel to the z-axis. Green lines trace the trajectories of scintillation photons, while yellow lines represent the paths of gammas.

through multiple Mie-scatterings of photons [53]. The light can then be collected close to the interaction of ionizing particles using optical fibers. This leads to an enhanced spatial resolution. Moreover, the reduced constraints on absorption properties as the light travels only a short distance to the fibers enable high loading in the scintillator offering flexibility in experimental setups. One of the most significant advantages of opaque scintillators is their ability to provide detailed topological information about the interaction within the detector. Unlike transparent scintillators, where light collection occurs at a larger distance from the interaction point, opaque scintillators allow for close light readout, preserving the energy deposition patterns of ionizing particles.

For instance, an electron produces a distinct, compact energy deposition pattern due to its short ionization path within the medium, appearing as a singular "blob" (bulky light object) in the detector. The typical size of such a blob is only a few centimeters. Conversely, gammas undergo multiple Compton-scatterings, resulting in a series of energy depositions along with a final photoelectric effect. Positrons, mimicking the behavior of both electrons and gammas, leave a trail of ionization similar to electrons before annihilating and emitting two back-to-back gammas with an energy of 511 keV. Each of the gammas produce then the characteristic Compton-scatter pattern. A simulation of the different topological patterns is shown in Figure 3.1.
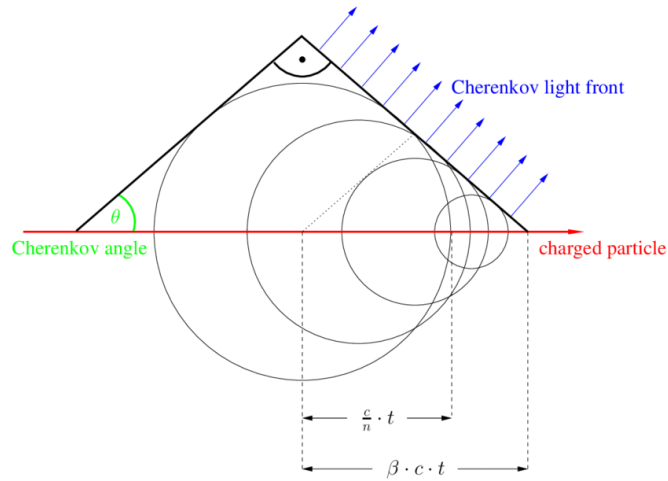
Fig. 3.2: Formation of a Cherenkov light cone if the charged particle travels faster than the medium speed of light. The picture is taken from [55].

3.1.2 Hybrid scintillator

When a charged particle traverses a dielectric medium, such as a scintillator, at a velocity greater than the speed of light in that medium, Cherenkov radiation is emitted [54]. The speed of light in a medium c_m is given by

$$c_m = \frac{c}{n},\tag{3.3}$$

where c is the vacuum speed of light and n the refraction index of the medium. As n is always larger than 1, the speed of light in the medium never exceeds the vacuum speed of light. In general, the refraction index is depending on the wavelength $n(\lambda)$.

On its way through a medium, the charged particle polarizes the atoms of the dielectric medium. If the velocity of the particle is faster than c_m, the polarization is asymmetric as the atoms cannot rearrange fast enough. During the depolarization of the atoms, electromagnetic waves are emitted. The constructive interference of these waves results in the formation of a distinctive cone of Cherenkov light, as illustrated in Figure 3.2.

The emission angle θ of the Cherenkov radiation relative to the direction of the charged particle is determined by

$$\cos(\theta) = \frac{1}{\beta n}\tag{3.4}$$

with $\beta = \frac{v_p}{c}$, where v_p is the velocity of the charged particle. The number of emitted photons N per path length ∂x and wavelength $\partial \lambda$ can be calculated with the Frank-Tamm formula [56]:

$$\frac{\partial^2 N}{\partial x \partial \lambda} = \frac{2\pi \alpha Z^2}{\lambda^2} \left(1 - \frac{1}{(\beta n(\lambda))^2}\right). \tag{3.5}$$

Here α denotes the fine-structure constant and Z the electric charge of the particle.

This leads to a different amount of produced Cherenkov light for different charged particles. Hybrid scintillators exploit this feature as particles or event types are discriminated based on the ratio of Cherenkov and scintillation light (C/S) [57]. For instance, electrons with sufficient high kinetic energy produce Cherenkov light. For a scintillator with a refraction index of $n = 1.48$, the kinetic energy threshold for an electron is $E_{th} \approx 0.2\,\mathrm{MeV}$. In contrast, gammas produce less Cherenkov light as they are uncharged and only deposit small amount of energies to electrons by Compton-scattering. For annihilation gammas with an energy of 511 keV, the energy of these electrons is too small to produce Cherenkov radiation, but higher energetic gammas can produce small amounts of Cherenkov light. Furthermore, positrons, while capable of producing Cherenkov light, exhibit a different ratio compared to electrons due to their annihilation resulting in the release of two gammas. These gammas do not produce Cherenkov light. For the same amount of scintillation light, positrons have a lower amount of Cherenkov light, because the kinetic energy of the positron is much lower than the one of the electron, as the total energy also includes the gammas.

Additionally, the combination of opaque and hybrid scintillator provides another method for background discrimination based on the blob-dependent Cherenkov scintillation ratio instead of the particle-dependent ratio explained before. This can be used to distinguish, e.g. a beta plus decay from a beta minus decay with simultaneous emission of a high energy gamma-ray from the de-excitation of the decay nucleus. The positron features a single blob with high Cherenkov to scintillation ratio from the ionization trail in the center of the chain blobs, as the annihilation gammas with no Cherenkov light are emitted back-to-back. In contrast, the simultaneous electron and gamma ray event features the blob with a high ratio at the beginning of the blob chain from the gamma ray.

There are several approaches for realizing a hybrid scintillator. The method planned for usage in NuDoubt^{++} is the slow hybrid approach, which uses intrin-

sically slow fluors and solvents for the scintillator [58]. The scintillation light is strongly delayed such that the small peak of Cherenkov light becomes visible at the beginning of the light emission.

3.2 OWL-fibers

The collection of the scattered scintillation light will be done with a dense grid of wavelength-shifting fibers. In NuDoubt++ new optimized fibers (OWL-fibers) based on novel wavelength-shifting modules (WOMs) developed for the IceCube-Upgrade [59] will be used, where the fiber is coated with the wavelength-shifter on the outside. Photons which hit the fiber are then absorbed from the wavelength-shifter and isotropically re-emitted at a higher wavelength. Photons which fulfill the condition for total internal reflection in the fiber will be guided to the ends, where they will be detected by SiPMs. Shifting the emission point of the photons to the outside of the fiber, increases the capture efficiency as more photons undergo total internal reflection [60]. Depending on the relation of the refractive index from scintillator and fiber material, improvement up to a factor of 4 compared to emission in the middle of the fiber are possible. One potential material for the OWL-fibers is polysterene. For a scintillator with refraction index of $n = 1.48$ the capture rate has a theoretical maximum of 38 % [61]. For the detection of the captured light silicon photomultipliers (SiPMs) are used, which are solid-state photodetectors that offer great sensitivity and versatility in detecting low-intensity light signals. SiPMs operate based on the principle of avalanche photodiodes, wherein incident photons generate electron-hole pairs within the silicon substrate. These charge carriers undergo multiplication via avalanche breakdown, resulting in a measurable electrical signal proportional to the incident light intensity. One of the key advantages of SiPMs is their high photon detection efficiency (PDE) compatible with PMTs, enabling the detection of single photons with high precision. The PDE strongly depends on the wavelength. The maximum is reached around 450 nm, where efficiencies between 30 % and 40 % are feasible [62]. Moreover, SiPMs exhibit excellent timing resolution in the range from 10 ps to 100 ps [63], allowing for precise temporal characterization of light pulses. This capability makes SiPMs especially well suited for the hybrid scintillation approach, where a high timing resolution is needed to separate Cherenkov and scintillation light. Additionally, SiPMs offer compact size, low power consumption and robustness

against magnetic fields, making them suitable for integration into many experimental setups. A disadvantage of SiPMs is the typically much higher dark current compared to PMTs.

3.3 Detector design

(a)

(b)
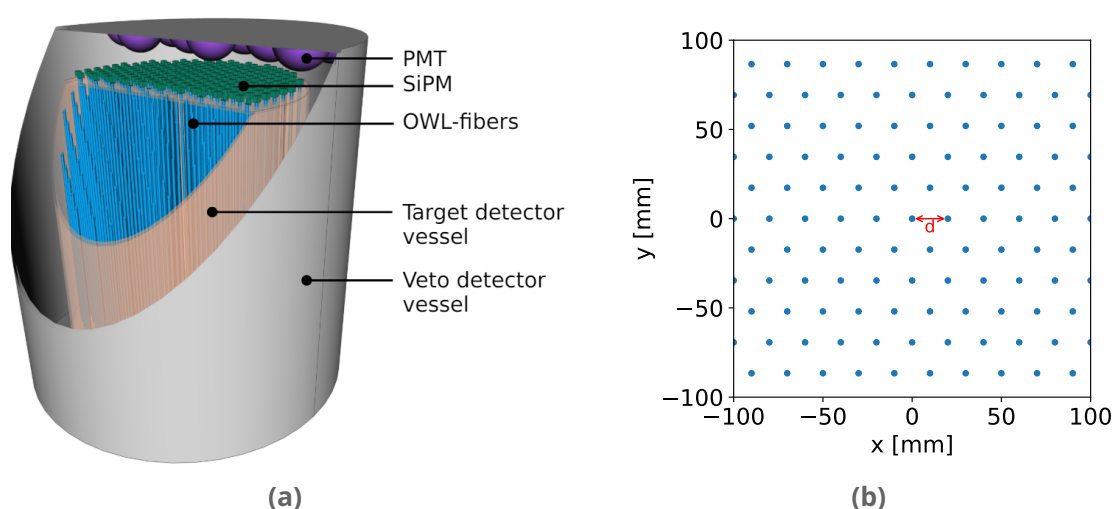
Fig. 3.3: (a) Basic detector design of the NuDoubt^{++} experiment [44]. The target detector vessel (orange) is filled with hybrid opaque scintillator and contains parallel running OWL-fibers (blue). Each fiber has one both ends SiPMs (green) for the readout of the fibers. The veto detector vessel (gray) contains transparent scintillator and has PMTs (purple) on the top and bottom to build an active veto. (b) excerpt of the triangular grid with spacing $d = 2\,\mathrm{cm}$.

The NuDoubt^{++} detector is designed with a cylindrical configuration, featuring a target detector vessel enveloped by an active veto detector, as depicted in Figure 3.3. The inner cylinder will contain approximately one metric ton of hybrid-slow opaque scintillator loaded with the isotope undergoing double beta decay. This cylinder will measure 110 cm in both height and diameter. Optimized wavelength-shifting fibers (OWL-fibers), running parallel to the symmetry axis, will traverse the cylinder. Each fiber will be coupled to silicon photomultipliers (SiPMs) at both ends for the readout. SiPMs at both ends lead to more collected light and thereby enhance the energy resolution crucial for detecting neutrinoless decay modes. The arrangement of OWL-fibers will be in a triangular grid, with the exact spacing

Tab. 3.1: Current limits for the half-lives of the positron emitting double beta decay modes of ^{78}Kr and ^{106}Cd [64, 65]. For the limits, the corresponding confidence levels, C.L., are listed. No measurements of these modes for ^{124}Xe have been done yet.

Isotope	$T_{1/2}(2\nu)$ [a]		$T_{1/2}(0\nu)$ [a]		C.L. [%]
	$\beta^+\beta^+$	ECβ^+	$\beta^+\beta^+$	ECβ^+	
^{78}Kr	$> 2.0 \times 10^{21}$	$> 1.1 \times 10^{20}$	$> 2.0 \times 10^{21}$	$> 5.1 \times 10^{21}$	68
^{106}Cd	$> 1.7 \times 10^{21}$	$> 2.1 \times 10^{20}$	$> 4.0 \times 10^{21}$	$> 1.2 \times 10^{21}$	90

yet to be determined. In this thesis, the impact of the spacing on both energy and spatial resolution is investigated.

Surrounding the inner cylinder will be an optically separated outer cylinder, which functions as an active veto. This outer volume, monitored by photomultiplier tubes (PMTs) and filled with transparent scintillator, is designed to be especially effective at detecting and vetoing neutrons.

3.4 Double beta decay isotopes

$\beta\beta$ decay is observable in isotopes for which the single β decay is energetically forbidden. There are 34 isotopes that are theoretically predicted to undergo $\beta^+\beta^+$, ECβ^+, or ECEC [32]. The NuDoubt^{++} experiment focuses on isotopes with high Q-values exceeding the gamma ray background of the ^{208}Tl decay ($E_{Tl} = 2.614\,\text{MeV}$) from the uranium/thorium decay chain, narrowing down the selection to three promising candidates: ^{78}Kr ($Q_{\beta\beta} = 2.881\,\text{MeV}$), ^{106}Cd ($Q_{\beta\beta} = 2.775\,\text{MeV}$) and ^{124}Xe ($Q_{\beta\beta} = 2.857\,\text{MeV}$). The half-life limits for these processes are listed in Table 3.1. To address the challenge of detecting rare double beta plus decay events, one can utilize the efficient enrichment of isotopes. Due to the long half-lives, many atoms of the isotope are needed to measure the decays. While the natural abundance of ^{78}Kr is relatively low (0.4 %), it can be enriched to over 50 %. Also ^{124}Xe has a low natural abundance of only 0.4 %, but can be efficiently enriched. Similarly, cadmium enrichment from 1.3 % to 66 % has been achieved [65].

Krypton can be loaded into the scintillator by bubbling the gas through it. According to Henry's law [66], increasing the gas pressure results in higher levels of krypton dissolved in the scintillator. As xenon is as well a noble gas, the isotope can be loaded into the scintillator in the same way as krypton. In the case of

cadmium, a compound can be dispersed throughout the wax-based scintillator, which is manufactured as liquid and operated as solid or a highly viscous state [52]. A highly refractive compound can also increase the opacity of the scintillator.

3.5 Background

The detection of $\beta^+\beta^+$ and ECβ^+ decays requires thorough control of the background sources, stemming from various processes with Q-values within the region of interest of the isotope under examination. Internal and external backgrounds both influence the experiment. Isotopes that can provide background due to β^+ decays in a similar energy range as the double beta decays under consideration are the carbon isotopes ^{10}C and ^{11}C. Furthermore, there are gamma emitting decays in this range from the uranium-thorium decay chain. A more detailed discussion on background events for the double beta decay of ^{78}Kr is given in Section 5.2.2.

Internal background arises from radioactive isotopes within the detector volume, such as the scintillator or the OWL-fibers. Radioactive contamination of the scintillator, including uranium and thorium, can be mitigated through purification efforts. Additionally, impurities within the OWL-fibers and dust on their surfaces contribute to the background.

External backgrounds encompass all energy depositions occurring within or close to the detector, originating from particles outside its volume. Cosmic muon-induced spallation on nuclei of the surrounding material or on nuclei within the detector, predominantly carbon, introduces significant background. This can be mitigated by deploying the detector deep underground to reduce cosmic muon flux effectively [67]. Furthermore, implementing a dedicated muon veto system around the target volume allows for efficient tagging of residual muons, enabling the use of time and spatial coincidences to veto spallation background [68].

These background sources are particularly pertinent for measuring the two-neutrino modes of double beta decays with a larger energy range. However, for the neutrinoless modes, only background within the small region of interest (ROI) matters. The ROI for neutrinoless double beta decay, defined as a narrow energy window around the monoenergetic peak at the Q-value, is determined by the energy resolution of the detector. For ^{78}Kr the ROI is between 2.821 MeV and 2.941 MeV. In the case of 0νECβ^+, the dominant background within the ROI

originates from spallation-produced carbon and gamma emissions from contamination of the OWL-fibers.

Combining opaque and hybrid scintillator technology can significantly diminish background levels, crucial for detecting such rare decays.

Reconstruction

4

This chapter focuses on the opaque scintillator component of the detector, utilizing a Geant4 simulation as detailed in Section 4.1. The primary objective is to develop a reconstruction method for determining the interaction position and energy within the scintillator. When a particle travels through the scintillator, scintillation light is generated and propagates through the opaque material to the OWL-fibers. By measuring the photons with the SiPMs, the energy and position of the event can be reconstructed. For simplification, the reconstruction is done for "photon bombs", which are a fixed number of photons starting from the exact same point within the scintillator. In particle events (e.g. electrons), the emission point is spread over a few millimeters as the electrons travel through the scintillator. For positrons, additional emission points from Compton-scattered electrons create multiple localized regions of scintillation light within the detector.

To achieve a reconstruction, it is necessary to formulate a method that describes the expected number of photons in each fiber based on the parameters to be reconstructed. One approach to this problem, using random walk properties, is discussed in Section 4.2 and Section 4.3. The reconstruction using a random walk model is examined in Section 4.4, whereas Section 4.5 addresses the shadowing effect that fibers have on each other, resulting in reduced photon counts in some fibers. Additionally, a method combining simulation and interpolation is outlined in Section 4.6. Furthermore, Section 4.7 examines the impact of different fiber arrangements and scintillator properties on the reconstruction performance.

4.1 Simulation

A simulation of the opaque scintillator cylinder for the NuDoubt^{++} experiment has been conducted using the GEANT4 simulation tool [69]. This simulation models the propagation of photons through the scintillator, accounting for Rayleigh scattering and absorption. The fibers are simplified as objects that "delete" all photons hitting them, while only "detecting" photons with a specified efficiency. This means

that only a limited number of the photons that hit the fibers are recorded as detected. This simplification allows for simulating the expected hits in a fiber without modeling the detailed propagation through the fiber and detection by the SiPM, which are responsible for the decreased efficiency. By deleting the photons upon contact with a fiber, it is ensured that no photon is detected multiple times. This is a realistic assumption given the high absorption efficiency of the wavelength-shifting paint on the fiber surface. Photons that are not captured by total internal reflection are highly unlikely to be detected by another fiber, as the absorption spectrum of the paint does not match the wavelength of the already shifted photons.

The Rayleigh scattering length, absorption length, and refractive index for optical photons can be specified, with these values assumed to be constant over the entire wavelength range. In reality, these parameters vary with wavelength. The scintillator is designed to have a light yield of 9000 photons per MeV. The scintillator is contained inside a cylinder with 110 cm height and diameter, which are the dimensions planned for NuDoubt^{++} . Some effects are not included in the simulation. For example, the absorption of Cherenkov light by the scintillator is not modeled. Cherenkov light covers a broad wavelength range, some of which overlaps with the scintillator's absorption spectrum. When this light is absorbed, it is re-emitted and measured as scintillation light. Additionally, the quenching effect in the scintillator is simplified by using a fixed Birks constant, as the exact quenching behavior of the scintillator is not known.

The simulation can handle photon bombs with a discrete number of photons starting from the same point as well as the signatures of real particles such as positrons or electrons, which produce Cherenkov and scintillation light. Additionally, the decay of isotopes can be simulated. For double beta decay, the GEANT4 BxDecay0 library is used to obtain the spectra of the decay products [70].

4.2 Random walk model

Light propagation in an opaque medium can be described by a random Walk [71]. In the following the description of a random Walk in the limit of a large step number is shown based on the work of Lord Rayleigh [72]. His approach is generalized to more dimensions as the photons can travel in all three spatial dimensions (Section 4.2.1). The model is then applied to the problem of light propagation in

an opaque scintillator and to the actual NuDoubt^{++} detector consisting of opaque scintillator with fibers traversing through it (Section 4.3).

The term random walk was first introduced in 1905 by Karl Pearson [71]. However, Lord Rayleigh applied this process earlier in 1880 to analyze a certain random vibration problem [72]. A random walk is a random process that describes a path that consists of a succession of random steps, often used as a model for various stochastic processes. Examples of the application are the Brownian motion of particles in a liquid [73], the search path of a foraging animal [74] and the stock fluctuating price [75]. Pearson gave a simple model to describe a mosquito infestation in a forest. At each time step, a single mosquito moves a fixed length a at a randomly chosen angle. He was interested in the distribution of the mosquitos after many steps has been taken. Lord Rayleigh found an asymptotic approximation if the step number approaches infinity $N \to \infty$ assuming a step length $a = 1$:

$$P_N(R) \sim \frac{2R}{N} e^{-R^2/N}. \tag{4.1}$$

$P_N(R)dR$ is the probability of traveling a distance between R and $R+dR$ in N steps. The expected distance traveled scales according to the square root of the number of steps, $\langle R \rangle \sim N$, which is typical for diffusion phenomena.

This approximation can be generalized to more dimensions and different step lengths, shown in the following based on [76].

4.2.1 Generalization to d dimensions

With a random walk one can calculate the probability density function (PDF) $p(\vec{r}, t)$ for a photon to be at position $\vec{r}$ at time t. Therefore, consider a random walker which starts at the origin in d dimensions. At each step, the walker moves by an amount of $\Delta \vec{X}_N$ described by a probability distribution $p_N(\vec{r})$. The steps are independent and $p_N(\vec{r}) = p(\vec{r})$. Additionally, an isotropic angular distribution is assumed, so that $p(\vec{r})$ is only a function of the radial distance $r = |\vec{r}|$.

Let $\vec{X}_N$ be the position of a walker after N steps, then there is the following recursion for the PDF $P_N(\vec{R})$ because of the independence of the steps:

$$P_{N+1}(\vec{R}) = \int p(\vec{r}) P_N(\vec{R} - \vec{r}) d^d \vec{r}. \tag{4.2}$$

As $N \to \infty$, $P_N(\vec{R})$ varies on much larger length scales than a typical $\vec{r}$, one can Taylor expand inside the integral:

$$P_{N+1}(\vec{R}) = \int p(\vec{r}) \left[P_N(\vec{R}) - \vec{r} \cdot \nabla P_N(\vec{R}) + \frac{1}{2}\vec{r} \cdot \nabla \nabla P_N(\vec{R}) \cdot \vec{r} + ... \right] d^d\vec{r} \qquad (4.3)$$

$$= P_N(\vec{R}) + \frac{\langle \vec{r} \cdot \vec{r} \rangle}{2d} \nabla^2 P_N(\vec{R}) + ... \qquad (4.4)$$

Now one assumes that steps are taken at intervals of Δt and gets:

$$\frac{P_{N+1}(\vec{R}) - P_N(\vec{R})}{\Delta t} = \frac{\langle r^2 \rangle}{2d\Delta t} \nabla^2 P_N + ... \qquad (4.5)$$

When $N \to \infty$, the limiting distribution $\rho(\vec{R}, t)$, defined by $P_N(\vec{R}) = \rho(\vec{R}, N\Delta t)$, satisfies the diffusion equation

$$\frac{\partial \rho}{\partial t} = D\nabla^2 \rho \qquad (4.6)$$

with the Diffusion constant

$$D = \frac{\langle r^2 \rangle}{2d\Delta t} \ . \qquad (4.7)$$

The walker starts in the origin, so the initial condition is $\rho(\vec{R}, 0) = \delta(\vec{R})$. This partial differential equation can be solved with a Fourier transform. With that, one obtains

$$\frac{\partial \hat{\rho}}{\partial t} = -Dk^2 \hat{\rho} \ . \qquad (4.8)$$

This ordinary differential equation has the solution

$$\hat{\rho}(\vec{k}, t) = e^{-Dk^2 t} \ . \qquad (4.9)$$

Taking the inverse Fourier transform gives

$$\rho(\vec{R}, t) = \frac{e^{-R^2/4Dt}}{(4\pi Dt)^{d/2}}, \qquad (4.10)$$

which is the probability density function for large number of steps (large times). This equation is also known as the Green's function of the random walk. In the corresponding discrete problem one gets

$$P_N(\vec{R}) \sim \frac{e^{-dR^2/2\langle r^2 \rangle N}}{(2\pi\langle r^2 \rangle N/d)^{d/2}}, \qquad (4.11)$$

as $N \to \infty$. This is the large step limit of $P_N(\vec{R})$ for an isotropic random walk in d dimensions. The PDF of the position tends to a normal distribution, whose width only depends on the variance of the individual displacements. For an isotropic walk, the PDF of the distance from the origin can be calculated by

$$P_N(R) = A_d R^{d-1} P_N(\vec{R}).$$
(4.12)

Here A_d is the surface area of the unit sphere in d dimensions. For Pearson's problem with $d = 2$ and $\langle r^2 \rangle = a^2 = 1$ equation (4.12) gives the asymptotic result of Lord Rayleigh (4.1).

4.3 Application of the random walk model in NuDoubt^{++}

These results can now be used for the light propagation in an opaque scintillator. In this case, one has $d = 3$ dimensions. The steps in the opaque medium are characterized by the scattering length λs. Every time a photon is scattered it changes its direction according to the angular distribution of the specific scattering phenomena.

4.3.1 Scattering mechanism

Light scattering in opaque scintillator can occur through two primary mechanisms: Mie scattering and Rayleigh scattering. Mie scattering describes the elastic scattering of light on particles with diameters similar to the wavelength of light, while Rayleigh scattering occursl when the size of the particles is much smaller than the wavelength (particle size $< 1/10$ wavelength [77]). These two mechanisms differ in their wavelength dependency and scattering angular distribution. Mie scattering tends to be more forward-directed than Rayleigh scattering. To illustrate, consider Figure 4.1, which depicts the scattering angular distribution for Rayleigh and Mie scattering. Since the exact scattering mechanism in the opaque scintillator is unknown, the simulation and calculation is done assuming Rayleigh-scattering due to its simplicity. The intensity of scattered light I_s by a small sphere of diameter
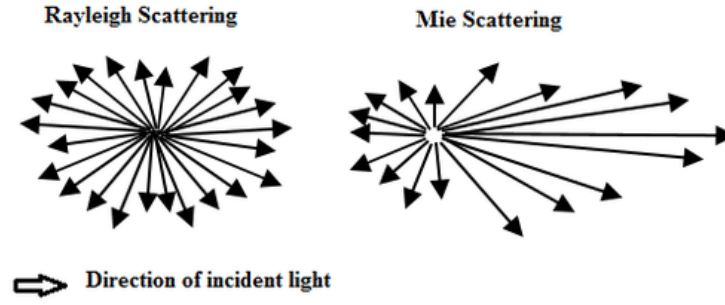
Fig. 4.1: Scattering angular distribution of Rayleigh and Mie-scattering [78].

d and refractive index n from a light beam with intensity I_0 and wavelength λ is given by the relation

$$I_s = I_0 \frac{1}{2R^2} \left(\frac{2\pi}{\lambda} \right)^4 \left(\frac{n^2 - 1}{n^2 + 2} \right)^2 \left(\frac{d}{2} \right)^2 \left(1 + \cos^2 \theta \right) \ . \tag{4.13}$$

Here, R is the distance to the particle and θ the scattering angle. Using Rayleigh scattering is well suited as Mie-scattering can be described and simulated with Rayleigh scattering using an effective scattering length.

Due to the small scattering length, light in opaque scintillators is expected to undergo multiple scatterings. The average cosine $\langle \cos(\theta) \rangle_n$ after n scattering events can be expressed in terms of the average cosine of the angle θ for a single scatter $\langle \cos(\theta) \rangle$ by

$$\langle \cos(\theta) \rangle_n = \langle \cos(\theta) \rangle^n \ . \tag{4.14}$$

Here, $\langle \cos(\theta) \rangle$ represents the anisotropy of scattering. If $\langle \cos(\theta) \rangle > 0$, scattering is preferentially in the forward direction (as is the case for Mie scattering). If $\langle \cos(\theta) \rangle = 0$ the scattering is forward-backward symmetric. This is the case for Rayleigh scattering and also for isotropic scattering.

The geometric scattering length λ_s, which represents the average distance between scattering events, can be considered the typical distance traveled between scattering events. However, for strongly forward-peaked scattering, an effective scattering length λ_e is more appropriate. This effective length, known as the transport mean free path, accounts for the tendency of light to preferentially scatter forward. The effective scattering length can be estimated using a statistical argument common in radiative transfer theory [79]. As light travels through a scattering medium, it undergoes multiple scattering events, with each step advanc-

ing along the initial direction by an amount determined by the average cosine of the scattering angle. By summing up these steps over many scattering events, one arrives at the total effective length of light transport

$$\lambda_e = \sum_{i=0}^{n} \langle \cos(\theta) \rangle^i .$$ (4.15)

For a large number of scattering events n, this becomes

$$\lambda_e = \frac{\lambda_s}{1 - \langle \cos(\theta) \rangle} .$$ (4.16)

Hence, as light propagates through a turbid medium the center of the photon cloud moves along the incident direction at a decreasing pace until it comes to a halt at a distance of λ_e from the point of injection. The effective scattering length thus serves a similar role for anisotropic scattering as the geometric scattering length does for isotropic scattering. Consequently, Mie-scattering can be effectively included in the model by using λ_e instead of λ_s.

Note that throughout the following discussion, the term scattering length λ_s is consistently used. However, when considering Mie scattering, it should be replaced with λ_e.

4.3.2 Light propagation

The light propagation in an opaque medium can be described by a random walk. For this purpose, the model derived in Section 4.2.1 can be used. This description is only valid, if the photons travel path lengths much larger than the scattering length λ_s, as only then the number of steps is sufficiently large. The model assumes isotropic scattering, which is appropriate for Rayleigh scattering due to its zero anisotropy. However, for Mie scattering, the effective scattering length must be used instead of the geometric one to account for anisotropy.

The probability density function for the path length before the next scattering is given by

$$p(r) = \frac{1}{\lambda_s} e^{-\frac{r}{\lambda_s}},$$ (4.17)

and thus only a function of the radial distance r. According to (4.7), the diffusion constant depends on the mean square displacement per step. This is given by

(a) x component

(b) y component

(c) z component

(d) $R = |\vec{R}|$
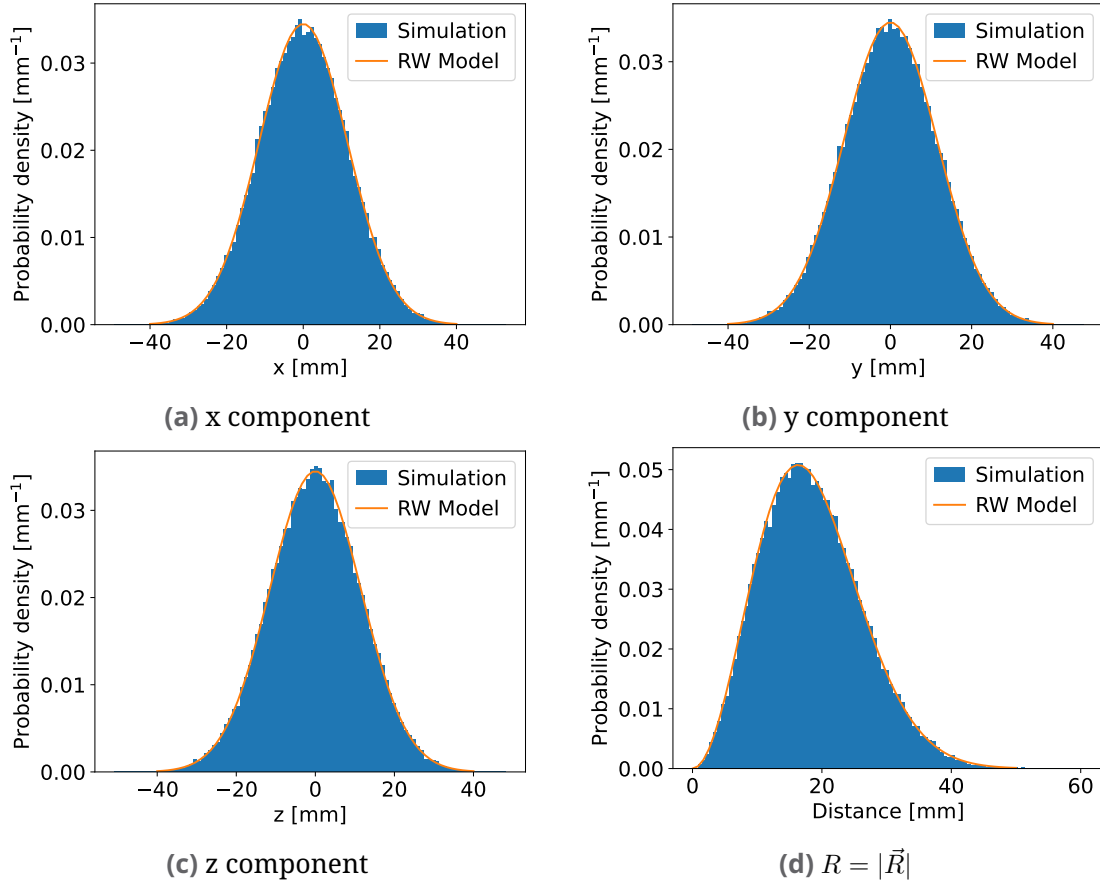
Fig. 4.2: Comparison of the random walk model with the simulation of the light propagation. The x, y and z component after $t =$ 1 ns is shown as well as the distance from the origin. The scattering length is 1 mm.

$\langle r^2 \rangle = 2\lambda_s^2$. The time step Δt can be replaced by $\Delta t = \langle r \rangle / v = \lambda_s / v$, where v is the velocity of the photons given by the speed of light c divided by the refraction index n ($v = c_0/n$). By putting this into (4.10), one obtains

$$\rho(\vec{R}, t) = \left(\frac{4}{3} \pi v \lambda_s t \right)^{-\frac{3}{2}} \exp \left(-\frac{3}{4} \frac{\vec{R}^2}{v \lambda_s t} \right). \tag{4.18}$$

To determine the distribution of the distance from the origin, one must multiply by $4\pi R^2$.

This theoretical model is validated through simulations of photons in Geant4, where their positions are tracked after a specific time t. Figure 4.2 compares the distribution obtained from the simulation to the theoretical model. In the simulation, the photons initially originate from the point (0,0,0).
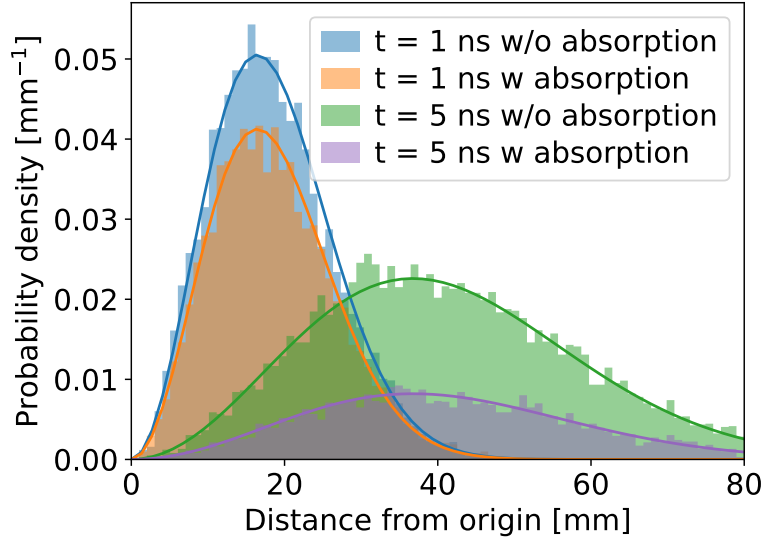
Fig. 4.3: Comparison of the model including absorption and the simulation for different times t. The light propagation is for both times simulated with and without absorption in the scintillator. The absorption length was set to 1 m and the scattering length to 1 mm.

In the scintillator the photons can not only be scattered but also absorbed. As the absorption length is much larger than the scattering length ($\lambda_a >> \lambda_s$), absorption can be added to the distribution of the position as a survival probability, which decreases exponentially with the path length. So (4.18) is modified to

$$\rho(\vec{R}, t) = \left(\frac{4}{3}\pi v \lambda_s t\right)^{-\frac{3}{2}} \exp\left(-\frac{3}{4}\frac{\vec{R}^2}{v \lambda_s t}\right) \exp\left(-\frac{vt}{\lambda_a}\right) \ . \tag{4.19}$$

In Figure 4.3, the model is again compared to the simulation, showing good agreement. Overall, the random walk model effectively describes light propagation in an opaque medium.

4.3.3 Integration of fibers into the random walk model

In addition to modeling the light propagation in the opaque scintillator, a comprehensive model for the NuDoubt^{++} experiment must also account for the optical fibers. When photons encounter the fibers, they are absorbed by the wavelength-shifting paint on the fibers. The absorption efficiency of the paint used for the WOM exceeds 99 % when used in air [59]. Although this efficiency decreases slightly

in the scintillator, it remains high enough to assume that all photons hitting the fibers are absorbed. Once absorbed, the photons are re-emitted at a different wavelength that lies outside the absorption spectrum of the paint. Consequently, photons absorbed once but not captured by total internal reflection cannot be absorbed again, simplifying the model by treating them as absorbed by the first fiber they encounter.

The fiber grid is spaced a few centimeters apart, which allows the model to be valid despite designed for many steps, as the scattering length is on the orders of millimeters. The primary goal of this modeling is to calculate the expected fraction of photons arriving at each fiber based on their initial position in the scintillator, which is crucial for event reconstruction. The fibers are aligned parallel to the z-axis. Therefore, measuring the photon count in a fiber does not directly provide information about the z-position where the photon originated. To achieve resolution for the z-position, the time difference between the SiPM at the upper and lower ends of the fibers can be analyzed. However, for the current purpose, the z-position is not considered. Instead the distribution from previous calculations (Equation 4.19) is integrated over z from $-\infty$ to ∞, since the fiber length is significantly larger than the scattering length in the scintillator (meters compared to millimeters).

Additionally, the starting position (x_0, y_0) of the photons is now included in the equation, whereas previous calculations assumed the photons originated at the origin. The distribution is also integrated over time t to determine the expected fraction of photons in the fiber at any time after their emission, rather than at a specific moment. This integration leads to the following distribution:

$$p(x, y, x_0, y_0) = C(\lambda_a, \lambda_s) K_0 \left(\sqrt{[(x - x_0)^2 + (y - y_0)^2] \frac{3}{\lambda_s \lambda_a}} \right).$$ \hfill (4.20)

Here, K_0 represents a modified Bessel function of the second kind. $C(\lambda_a, \lambda_s)$ denotes a normalization factor that depends on both the absorption and scattering lengths. This equation provides the expected fraction of photons at the point (x, y) for any arbitrary z-position. To determine the expected fraction of photons inside a fiber with radius r, this function must be multiplied by the fiber's effective area. Although mathematically correct to integrate over the fiber's area, a reasonable approximation can be achieved by simple multiplication, given the function's relatively slow variation over the area for small fiber radii. Consequently, an additional factor depending on the fiber radius r is included in Equation 4.20.

(a) Absorption length

(b) Scattering length
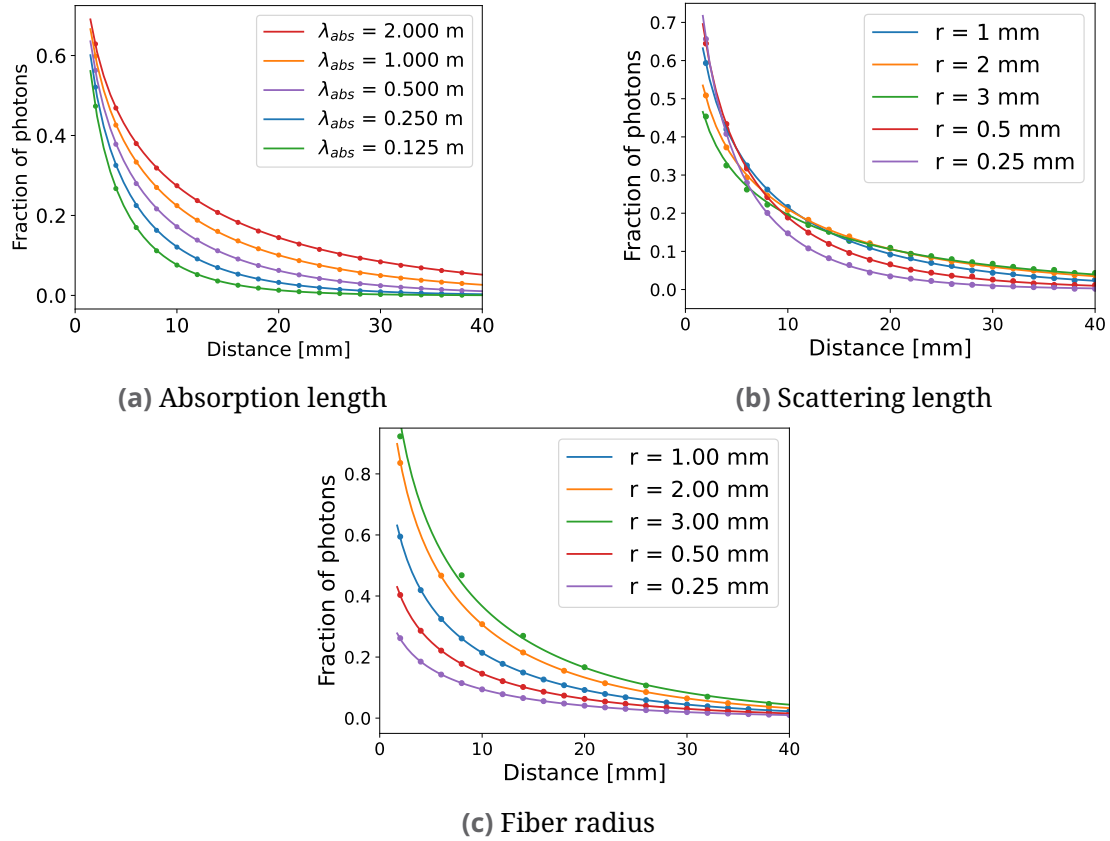
(c) Fiber radius

Fig. 4.4: Comparison of the simulation with the model using a fitted normalization factor C. The parameters varied are:(a) absorption length, (b) scattering length, and (c) fiber radius. In each case, the other parameters are fixed at $r = 1\,\text{mm}$, $\lambda_s = 1\,\text{m}$, and $\lambda_s = 1\,\text{mm}$. The Poisson uncertainty error bars are too small to be visible.

For simplicity, the normalization factor is not analytically calculated but instead obtained by fitting the model to simulation data with a χ^2 fit. In these simulations, fibers do not absorb photons but merely count those that arrive. This fitting process is repeated for various absorption lengths, scattering lengths, and fiber radii to derive an equation for the normalization factor based on these three parameters. The results, shown in Figure 4.4, compare the simulation data with the model using the fitted normalization factor, demonstrating good agreement. One can also see, that for a high fiber radius and a large scattering length, the model does not fit for small distances so good anymore, because there the assumption of a large number of steps before hitting a fiber is no longer fulfilled.

Until now, it was not considered, that the fibers absorb the photons and therefore photons that hit a fiber are no longer able to reach another one. In the part before,

(a) $x_0 = 6.5\,\text{mm}$, $y_0 = 4.5\,\text{mm}$ **(b)** $x_0 = 9\,\text{mm}$, $y_0 = 5\,\text{mm}$
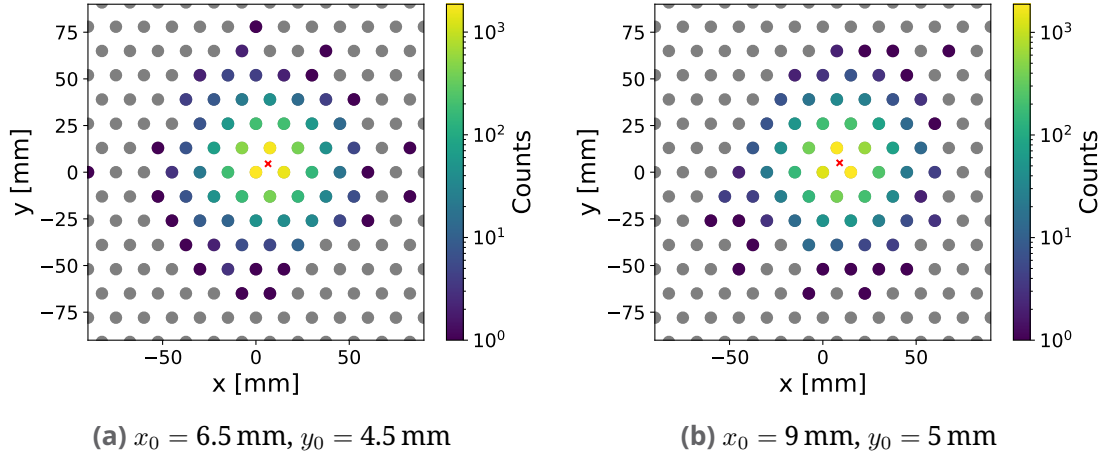
Fig. 4.5: Simulation results for two different starting points (indicated in red). Each initial photon bomb began with $N = 9000$ photons. The counts represent the number of photons arriving at each fiber, with fibers that received no photon hits shown in gray

the fibers counted only the photons. The fiber absorption is included into the model as an additional absorption length, leading to a combined effective absorption length:

$$\frac{1}{\lambda_a} = \frac{1}{\lambda_{a,\text{scint}}} + \frac{1}{\lambda_{a,\text{fiber}}} \, . \tag{4.21}$$

The assumption is made, that the fibers are far enough apart to be treated as a random absorption. Especially, it is assumed that each fiber influences all others in the same way.

Here again the model is fitted to simulation data, but this time with the real fiber grid with absorbing fibers. The test is done for a triangular grid with a spacing of 1.5 cm and a fiber radius of 1 mm. The scattering length is set to 1 mm and the scintillator absorption length $\lambda_{a,\text{scint}}$ to 1 m.

The simulation results for two different initial positions of photons are illustrated in Figure 4.5. The χ^2 fits for this data is shown in Figure 4.6. The reduced χ^2 values for the fits are 1.61 and 1.42, both of which are close to 1. This suggests that the fitted model accurately represents the simulation data, despite minor deviations observed primarily around 20 mm.

(a) $x = 6.5\,\text{mm}$, $y = 4.5\,\text{mm}$ **(b)** $x = 9\,\text{mm}$, $y = 5\,\text{mm}$
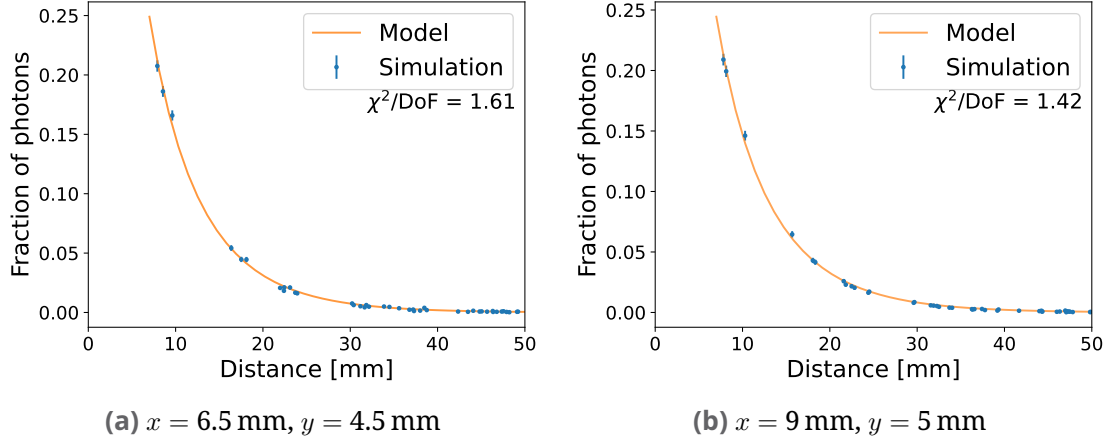
Fig. 4.6: Comparison from simulation including absorbing fibers with the random walk model for two different start points of photon bombs. The effective absorption length is fitted to the simulation data.

4.4 Reconstruction using the random walk model

Since the predicted photon counts from the model align well with the simulation data, the model is now applied for reconstruction. The reconstruction process utilizes the likelihood approach, as detailed in Section 2.3. Here, the measurements $\vec{n}$ consist of photon counts in each fiber. The parameters to be reconstructed are the initial photon start position, x and y, and the number of photons N. The number of photons is indicative of the energy of the particle that generated the photons, as the scintillator's light yield is approximately linear with respect to energy. Given that the measurements involve counting photons, a Poisson distribution is assumed, leading to the following likelihood function:

$$L(x, y, N | \vec{\mathbf{n}}) = \prod_{i=1}^{M} \nu_i(x, y, N)^{n_i} \, \frac{\exp(-\nu_i(x, y, N))}{n_i!} \,. \tag{4.22}$$

In this equation, $\nu_i(x, y, N)$ represents the expected photon count in each fiber, derived from Equation 4.20, and scaled by the number of initial photons N. The measurements are taken across M fibers, and it is currently assumed that all photons hitting a fiber are detected. However, in practice, due to the low capture efficiency resulting from total internal reflection in the OWL-fiber and the efficiency of the SiPM, only a fraction of the photons are actually measured.

(a) $x = 3.75\,\text{mm}$, $y = 6.5\,\text{mm}$, $N = 10\,000$

(b) $x = 2\,\text{mm}$, $y = -2\,\text{mm}$, $N = 10\,000$
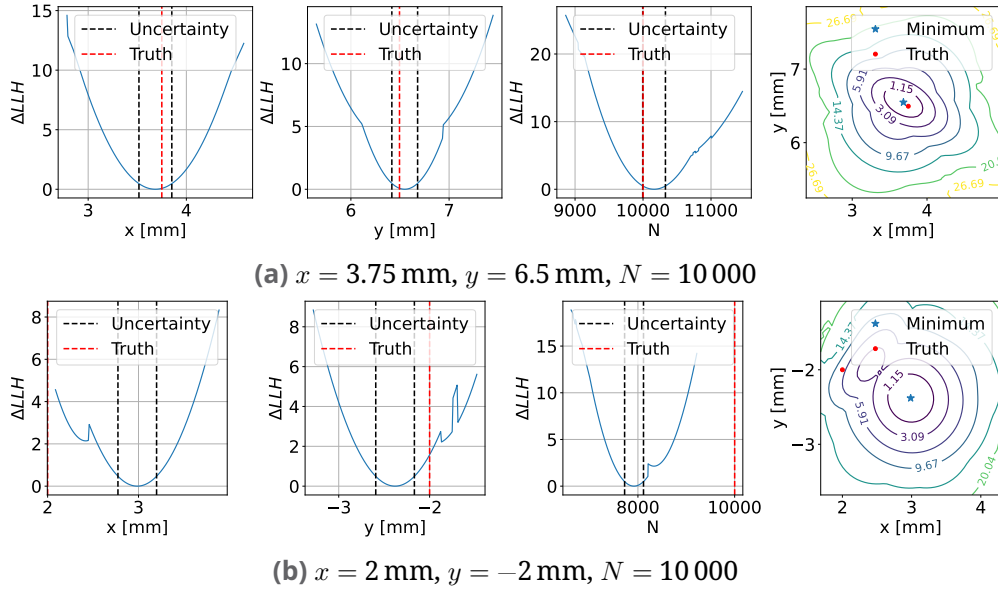
Fig. 4.7: Likelihood reconstruction using the random walk model for two different starting points of photon bombs. For each of the 3 parameters a 1D scan is shown, as well as a 2D scan of the x-y-plane. The different contours represent the 1 to 6σ confidence intervals.

The optimal parameters are determined by minimizing the negative logarithm of the likelihood function (LLH). For this minimization, the Nelder-Mead method, which is based on the simplex algorithm, is used [80]. In this initial test, the algorithm is initialized with the true parameter values. Figure 4.7 shows the results of likelihood parameter estimation for two different sets of true parameters. In the 1D likelihood profile scans, each parameter is varied within a small range while the likelihood function is minimized with respect to the other two parameters at each point. Similarly, in the 2D scan of the x-y plane, each point involves a minimization to determine N. The contours represent confidence intervals ranging from 1 to 6σ. In the profile scans, the uncertainty is indicated where the difference between the negative log-likelihood (LLH) value and the minimum equals 0.5.

In the first scenario, the photon start point is exactly midway between two fibers. Here, the reconstruction is accurate, with the true values well within the uncertainty range. In the second scenario, the start point is close to a fiber, resulting in poor reconstruction. While x and y lie within the 4σ interval, the reconstructed number of initial photons is significantly lower than expected, with the true value being strongly rejected. This discrepancy is observed in all reconstructions, except

for starting points within a small ($\sim 2\,\text{mm}$) radius around the midpoint between two fibers.

To investigate this discrepancy, the random walk model is compared to the simulation for different photon start points, as shown in Figure 4.8. For each point 10 000 photons are started. The model is fitted for photons starting midway between two fibers (shown in blue). For start points close to a fiber (e.g., shown in gray), the simple model fails to accurately describe the photon counts. Between 10 mm and 20 mm, the counts decrease much more steep than expected, but beyond 25 mm, the counts initially match the expected value before rising steeply again. This discrepancy is due to the shadowing effect of fibers on each other, where photons absorbed by one fiber cannot reach any other fiber. When another fiber is directly behind another one, the photon count is much lower than anticipated with the model. This effect is seen for the different "fiber rings" shown in orange and green in Figure 4.8b, corresponding to the steep decreases in photon counts. This indicates that the simplified model, which assumes counts depend only on the distance from the start point, is inadequate for start points close to the fiber. A more complex model, accounting for the location and orientation of the nearest fiber from the photon start point is necessary as this is the fiber most relevant for shadowing.

The following section examines the shadowing effect in more detail, investigating its impact on the measured photon counts.

4.5 Shadowing effect

The configuration of fibers plays a pivotal role in determining the amount of photons reaching each fiber. Fiber shadowing, where fibers obstruct each other's paths, result in diminished light reaching fibers located behind others. This can lead to different amount of photons at the same distance depending on the angle. The shadowing phenomenon complicates the simplistic model of a random walk with fibers merely extending the absorption length (c.f. Section 4.3.3). To delve into this effect, a detailed examination using simulations is conducted.

In this simulation, two distinct types of fibers are used: the conventional absorbing fibers, as encountered previously, possessing an absorption probability of 100 %, and newly introduced detection fibers. These detection fibers serve solely to tally arriving photons without absorbing them, providing a means to scrutinize the

(a) Photon counts

(b) Different start points
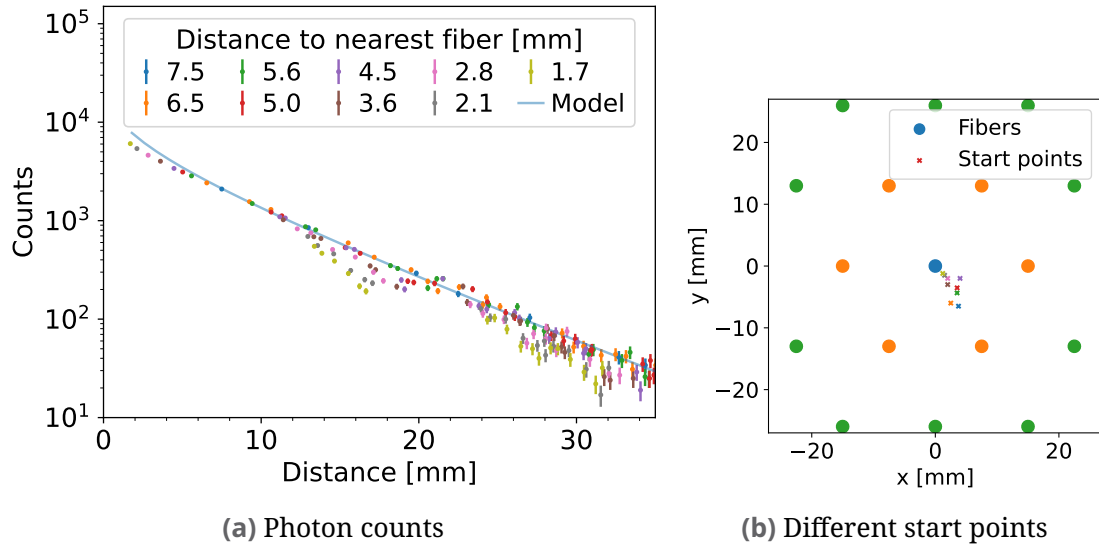
Fig. 4.8: Simulated counts in each fiber depending on the distance between start point and fiber for several different start points. The model is fitted for the case where the photons started in the middle between two fibers (blue). (b) shows the start points.

shadowing effects of absorbing fibers across multiple detection fibers concurrently. Each photon is only counted once per detection fiber. All fibers in the simulation exhibit a radius of 1 mm. The detection fibers are arranged in a circular configuration, with a radius denoted as R. Despite their proximity, the fibers do not overlap. Furthermore, an absorbing fiber is positioned at a distance r from the photon starting point, with α representing the angle between the detection fiber and the absorbing fiber (see Figure 4.9). The scattering length is set at 1 mm.

The shadowing effect is studied for two distinct radii R: 8 mm and 16 mm. A total of 100 000 photons are initiated at the center, and the investigation ensues into the number of photons reaching the detection fibers based on both their angle and the distance of the absorbing fiber.

The initial test focuses on discerning whether the fraction of arriving photons is uniform across all angles in the absence of an absorbing fiber. As depicted in Figure 4.10, fluctuations among the fibers fall within the bounds of Poisson uncertainty.
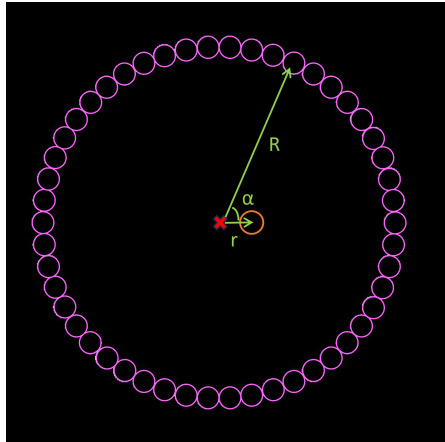
Fig. 4.9: Arrangement of the fibers in the simulation to study the shadowing effects. The absorbing fiber is depicted in orange, while the detection fibers are represented in pink. The red 'x' denotes the starting point of photons. All fibers have a radius of 1 mm and are aligned parallel to the z-axis, spanning a length of 2 m. Both the radius of the detection fiber ring, denoted as R, and the distance of the absorbing fiber to the starting point, denoted as r, are adjustable parameters.

(a) $R = 8\,\text{mm}$

(b) $R = 16\,\text{mm}$
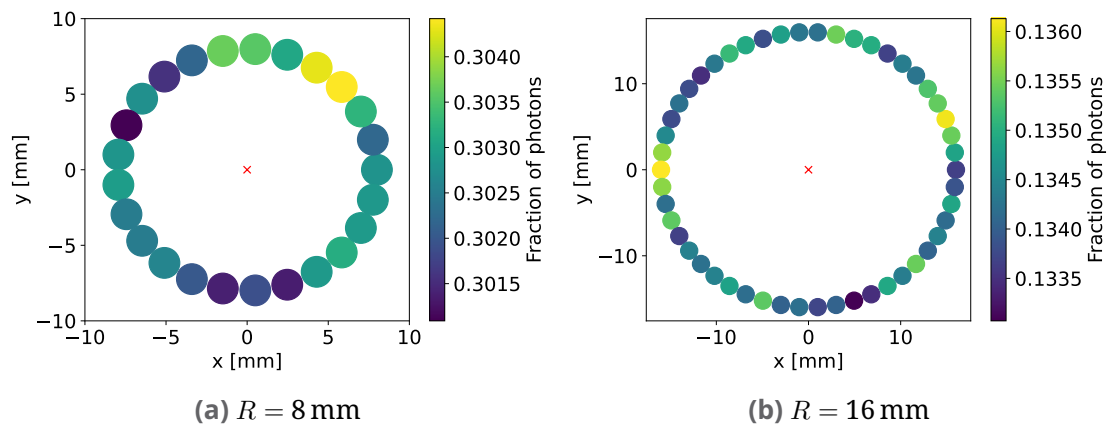
Fig. 4.10: Fraction of arriving photons at the detection fibers for two different radii R. No absorbing fiber for shadowing is included.

(a) $R = 8\,\text{mm}$, $r = 3\,\text{mm}$ **(b)** $R = 16\,\text{mm}$, $r = 9\,\text{mm}$
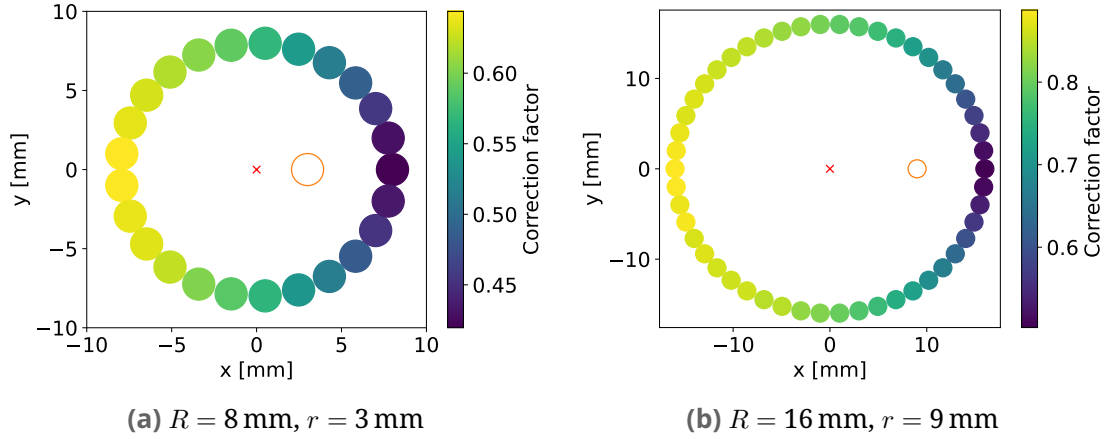
Fig. 4.11: Correction factor for varying distances to the absorbing fiber, r, and radii of the circle, R. The purple circle denotes the absorbing fiber.

To quantify the influence of an absorbing fiber, a correction factor c is introduced. This factor is defined as the ratio of the number of photons with an absorbing fiber N_{with} to the number without any absorbing fiber N_{without}:

$$c = \frac{N_{\text{with}}}{N_{\text{without}}} \, . \tag{4.23}$$

For N_{without}, the mean value across all angles is computed.

The correction factor is shown as an example in Figure 4.11 for various combinations of r and R. The impact of fiber absorption extends to all detection fibers, including those positioned at an angle of 180° relative to the absorbing fiber. Although the influence is minimal in this case compared to the other angles, for the configuration with $R = 8\,\text{mm}$ and $r = 3\,\text{mm}$ only slightly over 50 % of the photons without absorbing manage to reach these fiber. As anticipated, the most pronounced influence occurs directly behind the absorbing fiber (0°), where only approximately one-third of photons reach the detection fiber.

For more configurations the shadowing effect is shown in Figure 4.12. Here, for $R = 8\,\text{mm}$ and $R = 16\,\text{mm}$ the influence of the absorbing fiber is depicted relative to its distance. Note that this illustrations show the fraction of arriving photons rather than the correction factor. Notably, for larger distances r, the disparity among angles is most pronounced. Conversely, for smaller r, the discrepancy is less prominent, albeit resulting in a larger overall reduction in photon fractions.
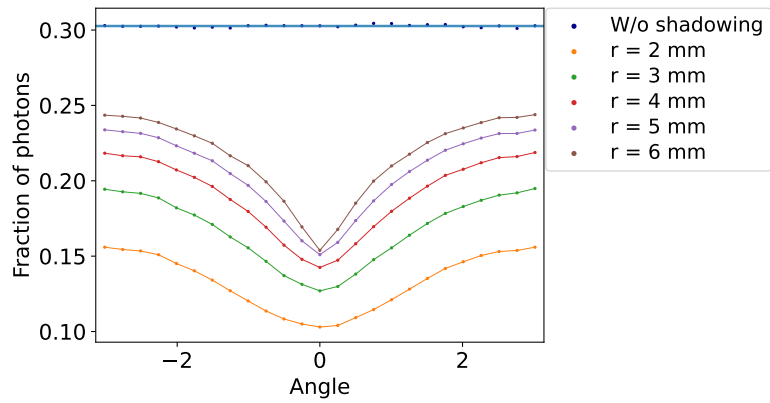
(a) $R = 8\,\text{mm}$
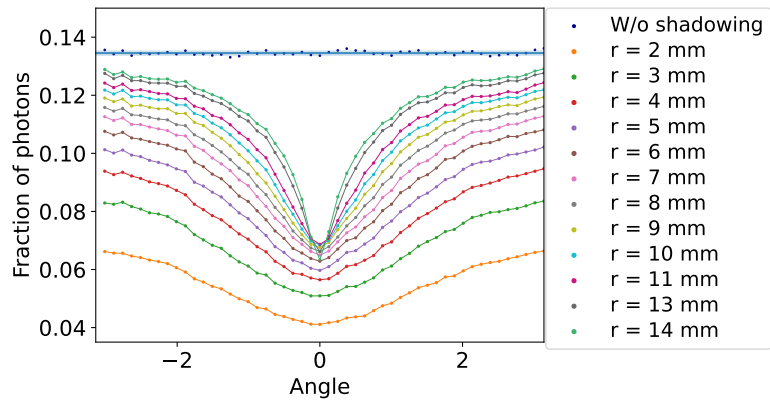
(b) $R = 16\,\text{mm}$

Fig. 4.12: Fraction of arriving photons at the detection fibers for different distances of the absorbing fiber compared to the scenario without absorption fiber.

4.5.1 Superposition of shadowing effects

In the fiber grid within the detector, numerous fibers are arranged, each capable of influencing others through shadowing effects. While the previous analysis focused on the impact of a single absorbing fiber, in the next investigation a second absorbing fiber is introduced. The aim is to explore whether one can simply combine the shadowing effects from each fiber individually. This would allow to correct the photon counts in the detector grid in an efficient way.

To explore the feasibility of a simple superposition approach for correcting the shadowing effects, simulations similar to those described previously are used. This time, an additional absorbing fiber was introduced within the circle of detection fibers, with the radius of the detection fiber circle set at $R = 20\,\text{mm}$. Two different arrangements of absorbing fibers are studied. Four simulations are performed: one without absorbing fibers, one with two absorbing fibers present simultaneously, and two separate simulations, each with one absorbing fiber individually. In each case, correction factors are computed based on the angle as done before.

To assess the validity of the superposition method, the expected photon counts for the scenario with both absorbing fibers are calculated by multiplying the correction factors obtained from each individual fiber:

$$N_{2\text{Fiber}} = c_1 \cdot c_2 \cdot N_{\text{without}}\,, \tag{4.24}$$

where N_{without} represents the photon counts without any absorbing fibers. The comparison between these calculated values and the simulation results with two absorbing fibers is depicted in Figure 4.13. The approach was tested for two different absorption fiber arrangements. Here, the color scale illustrates the relative difference between the calculated and simulated values. In both configurations, maximum deviations of about 10 % are observed. Notably, in one configuration (Figure 4.13b), the calculated values were consistently lower across almost all angles, while in the other configuration, there were detection fibers where the calculated values exceeded the simulation results.
Despite these discrepancies, the overall deviation appears sufficiently small to warrant consideration of the superposition method for correcting photon counts in the actual fiber grid.

(a) $r_1 = 14.4\,\text{mm}$ and $r_2 = 8.6\,\text{mm}$ (b) $r_1 = 8.6\,\text{mm}$ and $r_2 = 5.3\,\text{mm}$
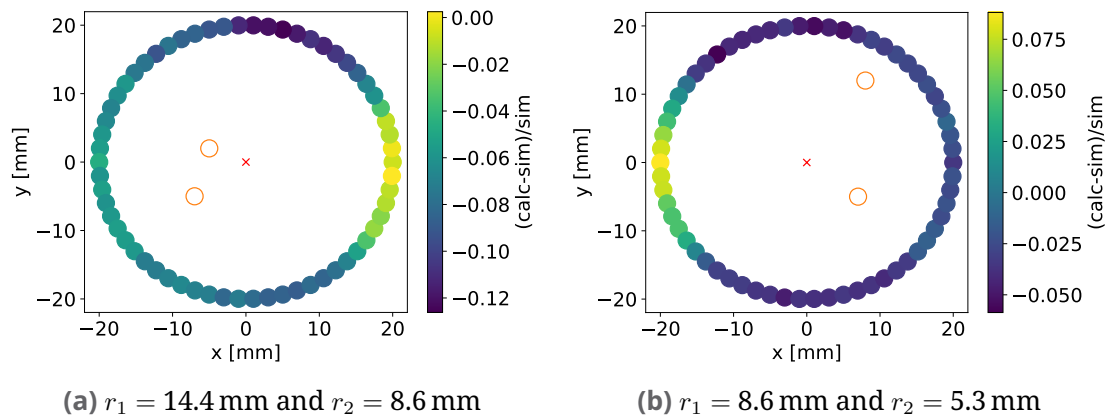
Fig. 4.13: Comparison of the amount of photons arriving at the detection fibers from simulation with the amount from the superposition calculation for two different arrangements of the absorbing fibers. The black circles represent the absorbing fibers.

4.5.2 Correction of the random walk model with shadowing effects

As the superposition approach to calculate correction factors in presence of multiple absorbing fibers seems to work, the approach is now applied to the hexagonal fiber grid of the NuDoubt^{++} detector. A fiber spacing of 20 mm and fiber radius of 1 mm is used.

Therefore, for the fiber where one wants to know the photon count one needs the correction factor from all other fibers individually to multiply them. This factors depend on the position where the photons start, as then the angle between the shadowing fibers and the one one looks at changes as well as the distances. In Figure 4.14a, the parameters relevant for the correction factor are illustrated: R, r and α. This already shows that there are a lot of combinations of these parameters when allowing a random start point. As it is impossible to simulate the correction factor for all combinations, a large number is simulated and then the factors are interpolated to get values for each combination. For this R and r are changed between 0 and 15 cm. The interpolation in this three dimensional parameter space is done using radial basis function interpolation [81]. The performance of this interpolation is shown in Figure 4.14b. There the predicted factor from the interpolation is compared to the factors obtained from simulation. This is done for events not included in the interpolation. As can be seen, except a few outliers the prediction matches pretty well the simulation results, which indicates a good interpolation.
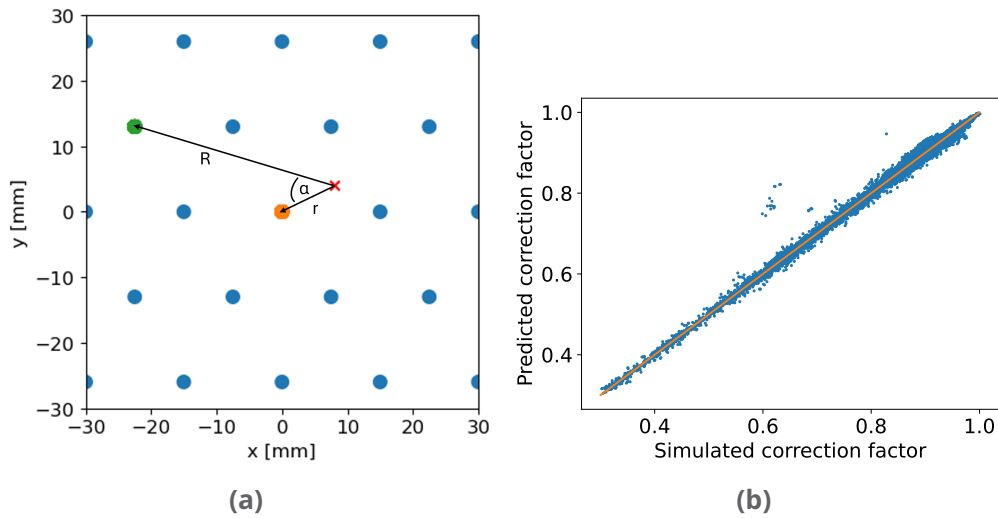
Fig. 4.14: (a) Illustration of the superposition approach. The red 'x' denotes the start point of the photons. To calculate the correction factor for the counts in the green fiber, the factors of all blue and orange fibers are multiplied. As an example, the parameters for the factor of the orange fiber are shown. (b) Comparison of the simulated correction factor with the predicted one from the interpolation. For the check, simulation data points which are not included in the interpolation, are used.

Now the shadowing correction is applied to the model calculating the expected amount of photons in each fiber. This is done for two different start points of the fibers, one corresponding to a point near to the mid point between two fibers and one pretty close to a fiber. The comparison from this calculation with the simulation results is shown in Figure 4.15. There are a lot of deviations between the calculation and the simulation, especially in the fibers far away. Notably, for the start point in the middle the calculation gives in most of the fibers a too low photon count. This is kind of expected, as the superposition of the shadowing effects does not include that photons which are already shadowed from one fiber cannot be absorbed in another one. Contrary, in the other case the calculation remains too high.

Overall, no enhancement of the random walk model was attained through this method, underscoring the necessity for an alternative approach to predict photon counts based on the start point.

(a) $x = 9.55\,\text{mm}$, $y = 2.16\,\text{mm}$ (b) $x = 1.08\,\text{mm}$, $y = 1.92\,\text{mm}$
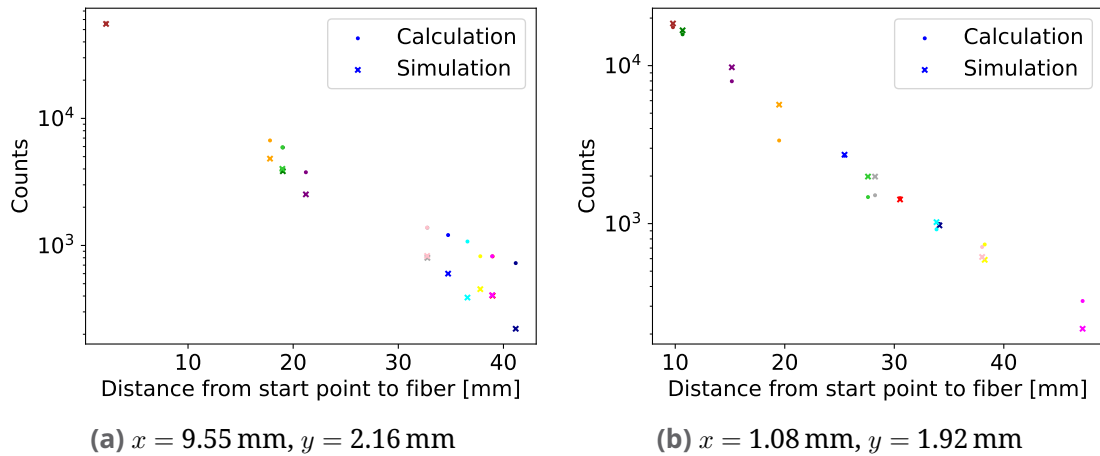
Fig. 4.15: Comparison of the predicted counts from the shadowing effect correction with the simulation for two different start points of the photons. (a) shows a start point near to the middle between two fibers, (b) a start point really close to a fiber. The fiber spacing is 20 mm and the fiber radius 1 mm.

4.6 Reconstruction using interpolation

Since no satisfying results were achieved with the random walk model, a purely simulation based approach is chosen. Therefore, events covering the whole parameter space were simulated and the results have been interpolated. For the reconstruction, the same likelihood function as before (Equation 4.22) is used, where the expectations $\nu_i(x, y, N)$ are obtained from the interpolation now and not from the Random walk model. The relevant parameters for the interpolation are discussed in Section 4.6.1. The reconstruction performance for photon bombs is shown in Section 4.6.2. Section 4.6.3 presents the Asimov approach for evaluating reconstruction performance.

4.6.1 Interpolation

The goal of the study is to determine how different detector geometries and scintillator properties influence reconstruction performance. To achieve this, an interpolation is created that depends on these parameters. From the shadowing effect study, it is known that the counts in a fiber not only depend on its distance to the photon source but also on the orientation and distance of the nearest fiber. This results in the following seven parameters for the interpolation:

- Scattering length of the scintillator λ_s

- Absorption length of the scintillator λ_a

- Fiber radius r_F

- Distance between fibers in triangular grid d_F

- Distance from source to fiber R

- Distance from source to nearest fiber r

- Angle between fiber and nearest fiber α

A visualization of the last three parameters is shown in Figure 4.14a. For the interpolation, simulations were conducted for several combinations of λ_s, λ_a, r_F, and d_F. The scattering length was varied in 6 steps between 0.5 mm and 8 mm, the absorption length 6 steps between 0.5 m and 5 m, the fiber radius 3 steps between 1 mm and 3 mm, and the distance between fibers between 1 cm and 5 cm in 5 steps. To cover the entire parameter space of r, R, and α, The photon sources were varied within a small region of the detector, which is representative of the entire detector due to its repetitive symmetry. 15 source positions have been simulated for each combination of the other parameters. As an example, the photon source positions for $r_F = 1$ mm and $d_F = 1$ cm are shown in Figure 4.16a. For each start point, 10 simulations were conducted, each with one million photons, to have a small statistical uncertainty. The fraction of photons arriving at the fibers was averaged over the 10 simulations for each combination. The results were then interpolated using radial basis function interpolation. The quality of this interpolation is shown in Figure 4.16b, where the predicted fraction is compared to the simulated fraction for events not included in the interpolation.

It is assumed that all photons hitting a fiber are detected. To obtain the actual number of expected measured photons, reflecting the expected efficiency of the SiPMs and accounting for losses in the OWL-fibers.

4.6.2 Reconstruction performance

To evaluate the reconstruction performance, 1000 photon bombs, each containing 10 000 photons, were simulated at a fixed position in the detector ($x = 5.86$ mm, $y = -7.58$ mm). Unless otherwise specified, a "standard" detector configuration of scattering length $\lambda_s = 1$ mm, absorption length $\lambda_a = 2$ m, fiber radius $r_F = 1$ mm
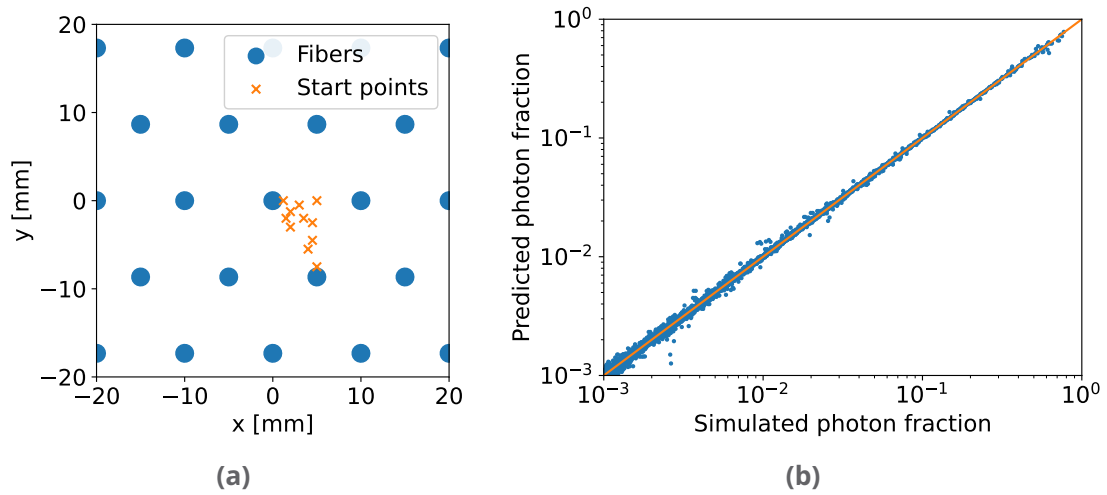
Fig. 4.16: (a) Start points of the photon bombs in the configuration with fiber radius $r_F = 1$ mm and fiber spacing $d_F = 1$ cm. One start point is chosen directly at the edge of a fiber to cover the total space. (b) Comparison of the simulated photon fraction with the predicted one from the interpolation. For the check, simulation data points which are not included in the interpolation, are used.
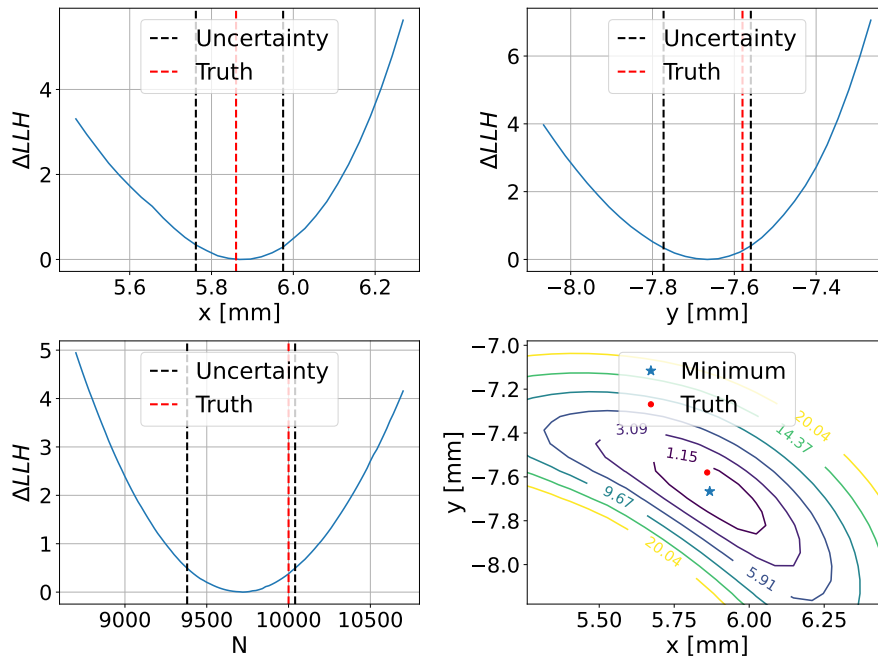
Fig. 4.17: Likelihood reconstruction using the interpolation for true parameters $x = 5.86$ mm, $y = -7.58$ mm, N $= 10\,000$. Profile scans for each parameter and a 2D scan of the $x - y$-plane is shown. The contours represent the 1 to 6σ confidence intervals.
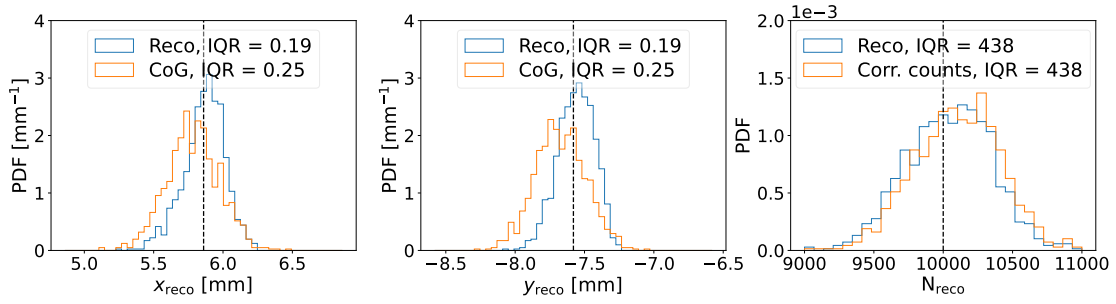
Fig. 4.18: Reconstruction performance at $x = 5.86\,\text{mm}$, $y = -7.58\,\text{mm}$, $N = 10\,000$. The true parameters are indicated with the vertical lines. For comparison, the center of gravity is shown for x and y and the corrected number of total counts for N.

and fiber distance $d_F = 1\,\text{cm}$ is used in the following. Notably, the fiber efficiency is set to 9 %, necessitating scaling down the expectation values derived from interpolation. For each simulation at the fixed point, a likelihood reconstruction is performed using expectation values from the interpolation. An example of such a likelihood scan is depicted in Figure 4.17.

To minimize the negative log-likelihood, the Nelder-Mead algorithm is used with x and y initialized at the center of gravity calculated from the measurements. In the center of gravity the fiber center positions (x_i, y_i) are added up weighted by the counts n_i in each fiber divided by the total number of counts. For the seed of N the total number of counts is corrected by the fiber efficiency of 9 % and additionally with the expected fraction of absorbed photons in the scintillator for the specific detector configuration. These values are determined from simulation data used in interpolation, averaging the number of total counts for each configuration. These seeds lead to similar results as it is the case for seeding at the truth values, so these are good values for real measurements where the true parameters are unknown. Figure 4.18 illustrates the results of all reconstructions at the fixed point. The interquartile range, defined as the difference between the 75th and 25th percentiles of the reconstructed parameter distributions, quantifies their width. Seed values' distributions are also shown for comparison. At this fixed point, a positional resolution of 0.19 mm is achieved. The center of gravity serves as a reasonably accurate estimator for x and y, although broader than the reconstruction with a width of 0.25 mm. The center of gravity distribution is slightly biased toward the nearest fiber, which in this case is located at $(5, -8.66)$, while the reconstruction exhibits no such bias. Regarding the photon number N, both the reconstruction
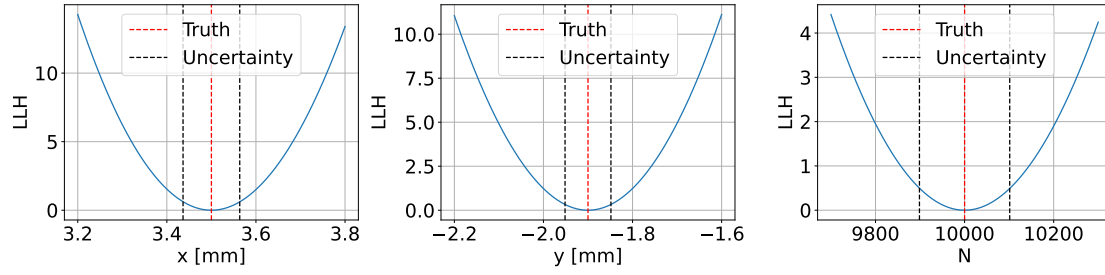
Fig. 4.19: Likelihood scans using the Asimov data set. The minimum is always at the true parameters.

and corrected counts have a width of 438 photons, slightly biased toward higher photon numbers.

This study shows the reconstruction performance at a single fixed point. To generalize across the detector, reconstructions at various points are necessary due to potential positional dependency. The Asimov approach offers a method to approximate resolutions across the detector without the need for extensive simulations.

4.6.3 Asimov approach

To investigate the reconstruction performance one can use Asimov data [82], which significantly reduces simulation effort. Typically, thousands of simulation data would need to be generated for a given set of parameters, and the reconstruction performance would be determined from the distribution of these reconstructed parameters. However, the Asimov approach defines a single representative event using expected photon counts for the true parameter set. In the likelihood function (Equation 4.22), the measurements $\vec{n}$ are replaced by the expectation values $\nu_i(x_{\text{true}}, y_{\text{true}}, N_{\text{true}})$.

$$L_{\text{Asimov}}(x, y, N) = \prod_{i=1}^{M} \text{PMF}_{\text{Poisson}}(\nu_i(x_{\text{true}}, y_{\text{true}}, N_{\text{true}})|\nu_i(x, y, N)) \qquad (4.25)$$

Here, PMF stands for the probability mass function of the Poisson distribution. By construction, the minimum of this likelihood function is at the true parameter values. The parameter uncertainties can be extracted from likelihood profile scans, with an LLH value of 0.5 marking the boundaries of the 68 % confidence interval (Figure 4.19). In the Asimov approach, this uncertainty range is assumed to be a good estimator for the actual range of reconstructed parameters.
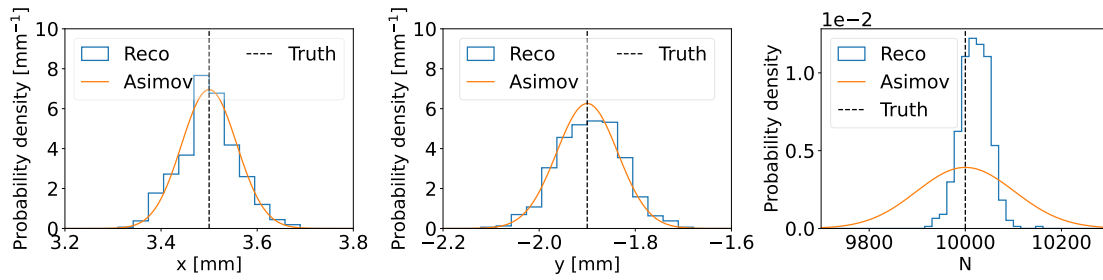
Fig. 4.20: Comparison of the reconstruction with the curves obtained using the Asimov approach.
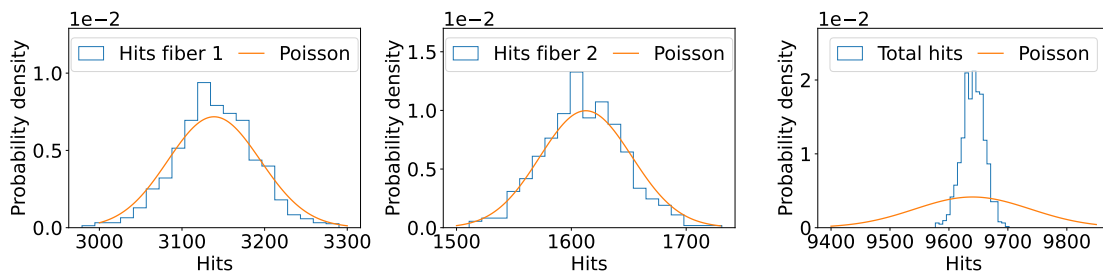
Fig. 4.21: Comparison of registered hits in two neighboring fibers and the total hits with a Poisson distribution. Hits refers to the number of photons arriving at a fiber, not the actual measured number of photons taking into account the fiber efficiency.

To validate this method, 1000 events with $x = 3.5\,\text{mm}$, $y = -1.9\,\text{mm}$, and $N = 10\,000$ are simulated and reconstructed. The distribution is then compared to the Asimov curves in Figure 4.20. Here, the LLH value was first multiplied by -1. The exponential of these values (exp(-LLH)) was then taken and normalized to create the probability density function, which can be compared to the distribution from the reconstruction. While the x and y curves align well with the reconstruction, the N curve is much broader, indicating that the reconstruction performs better than the Asimov approach predicts.

This discrepancy arises because the assumption of a Poisson PDF for the counts in each fiber is not entirely accurate. While it holds for individual fibers, the total number of counts is not Poisson distributed. This effect is illustrated in Figure 4.21, where the number of registered hits in two fibers from 1000 simulations is compared to a Poisson distribution, showing good agreement. However, the total number of registered hits deviates significantly from a Poisson distribution. The reason, fo the total number of hits not being Poisson distributed is due to inter-dependence of counts in individual fibers. It is impossible for all fibers to register
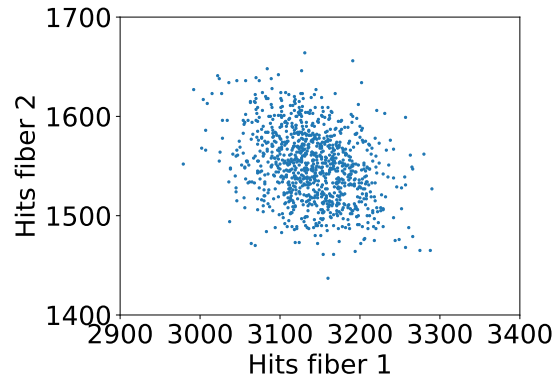
Fig. 4.22: Number of registered hits in two nearby fibers. There is an anti correlation with a correlation coefficient of -0.35 between them.

more photons than expected because the total number of photons is limited. In the same way, it is not possible for all fibers to see too little light. This anti-correlation between nearby fibers is shown in Figure 4.22, where a correlation coefficient of -0.35 is found for hits in two neighboring fibers. This correlation is not accounted for in the likelihood function, as each fiber's contribution is considered independently. Consequently, for the number of initial photons, the Asimov approach is inadequate and the ratio between the reconstruction width and Asimov width depends on the correlation strength. In a denser grid, the correlation between fiber is higher than for high distances between the fibers.

4.7 Influence of detector properties on reconstruction performance

In the following study, the impact of various detector properties on the reconstruction performance is examined. The parameters investigated include the absorption and scattering length of the scintillator, the fiber radius, and the distance between fibers. Each parameter is varied individually while keeping the others fixed at standard configuration values ($\lambda_s = 1\,\mathrm{mm}$, $\lambda_a = 2\,\mathrm{m}$, $r_F = 1\,\mathrm{mm}$, $d_F = 1\,\mathrm{cm}$). The performance is analyzed by simulating 1000 events at random positions in the detector. The number of photons is fixed at 9000, corresponding to the light yield of electrons and positrons with an energy of $1\,\mathrm{MeV}$. To obtain realistic results, the fiber efficiency is set to $9\,\%$.

The distributions for the standard configuration are shown in Figure 4.23. The interquartile range (IQR) of the position distributions is 0.27 mm, and for the number of photons, it is 370. The uncertainty on the IQR values is obtained using bootstrapping [83]. Figure 4.24 shows the IQR values for different detector configurations.
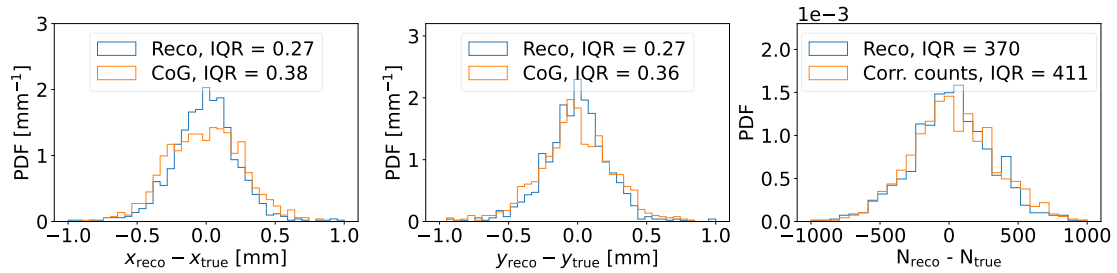
Fig. 4.23: Reconstruction performance for the "standard" configuration, illustrating the difference between reconstructed and true parameters. Simulations for 1000 photon bombs originating from random start points within the detector were conducted, with the number of photons fixed at $N = 9000$. For comparison, the center of gravity is shown for x and y and the corrected number of total counts for N.

Increasing the distance between the fibers worsens the resolutions. The position resolution decreases from 0.27 mm at 1 cm spacing to 1.10 mm at 30 mm. The number of photons can be reconstructed with a precision of 380 photons for low fiber distance and only 540 at 30 mm.

The fiber radius has minimal impact on reconstruction at a low scattering length of 1 mm because the high scattering probability ensures photons reach the fibers even if they are small. Smaller fiber radii are advantageous as they use less material, reducing the radioactive contamination in the detector. Additionally, less space is consumed from the fibers leaving more volume for the scintillator containing the double beta isotope.

The absorption length also has a minor influence. Figure 4.25 shows the fraction of photons reaching any fiber for different absorption lengths and fiber distances. In the standard configuration (1 cm spacing and 2 m absorption length), over 96 % of photons reach a fiber. For an absorption length of 1 m, this decreases to 92 %. As almost all photons hit a fiber with an absorption length of 2 m, further increases do not significantly impact reconstruction. Only at 1 m there is a slight performance decline.

The last parameter examined is the scattering length. Here, the resolution decreases with larger scattering lengths, as confining the light in a small volume
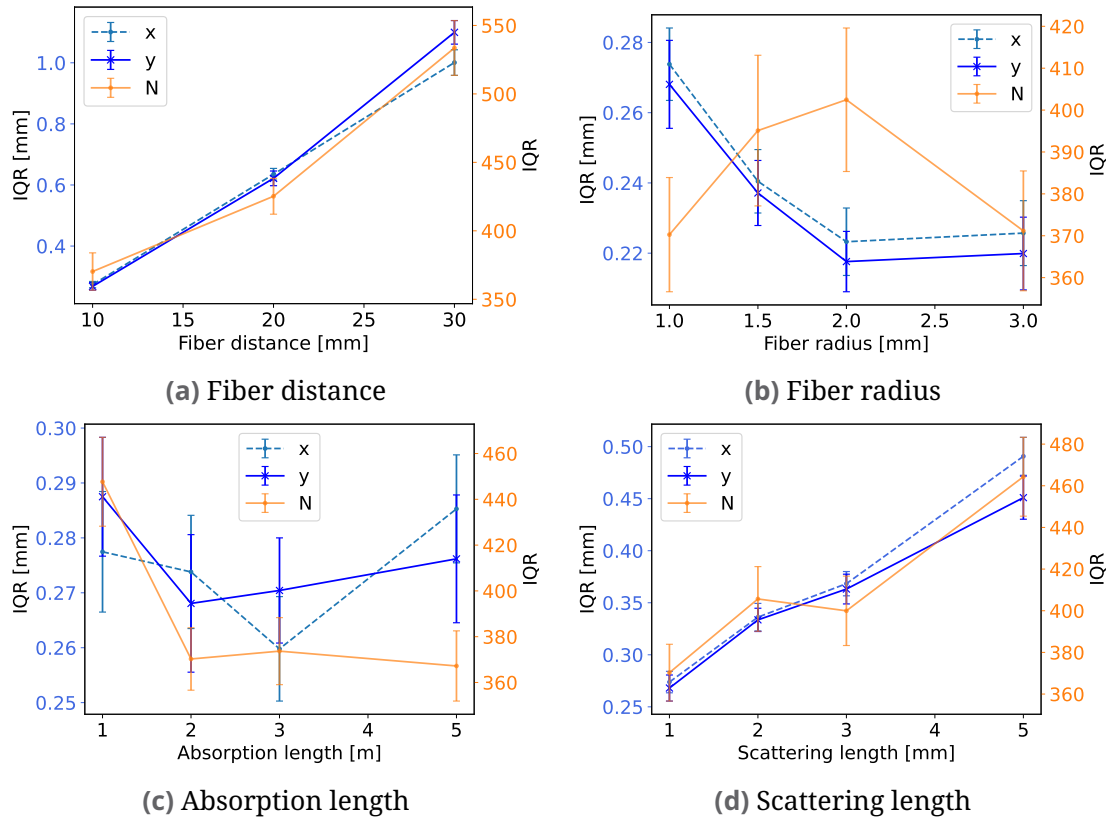
Fig. 4.24: IQRs of the reconstructions depending on different parameters of the detector configuration. All other parameters are fixed at the values from the "standard" configuration ($\lambda_s = 1\,\mathrm{mm}$, $\lambda_a = 2\,\mathrm{m}$, $r_F = 1\,\mathrm{mm}$, $d_F = 1\,\mathrm{cm}$). The uncertainties are calculated using bootstrapping.

using high scattering probability is advantageous. Larger scattering lengths allow photons to travel greater distances without hitting a fiber, resulting in fewer photons near the origin.

Finally, the influence of the number of photons on the resolution is checked for the standard configuration. The number of photons indicates the particle energy, as the light yield of the scintillator is approximately linear with energy. As expected, the resolution decreases with fewer photons. For N, the IQR divided by the number of photons is given. At $N = 9000$ this value is at $4\,\%$, while at $N = 1000$, it more than doubles.
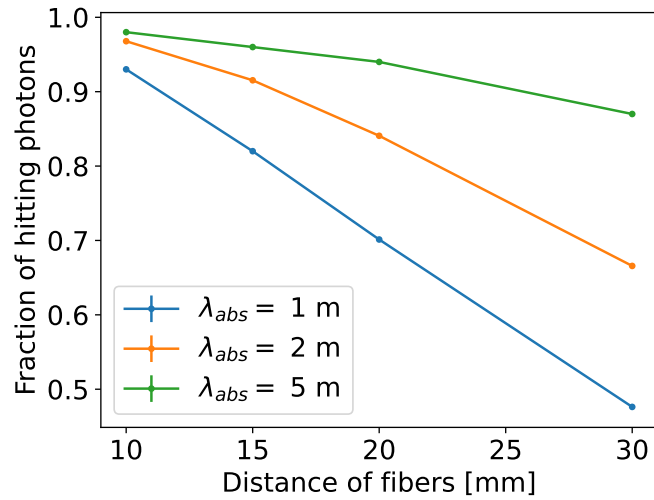
Fig. 4.25: Fraction of photons reaching a fiber depending on the fiber distance for different absorption lengths.
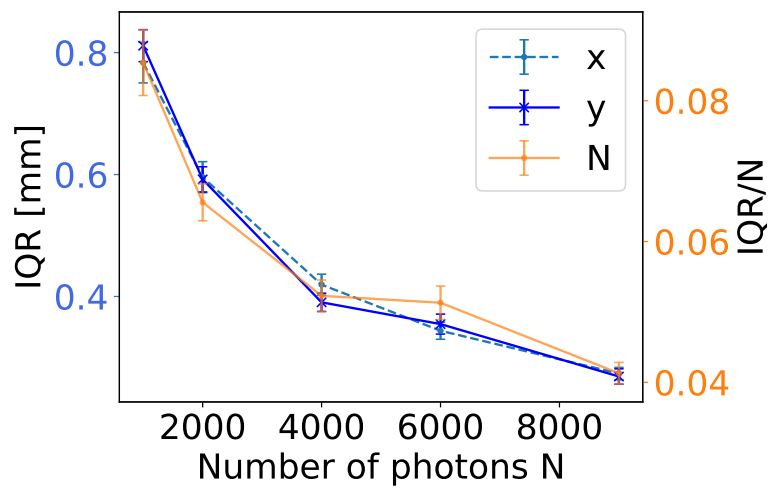
Fig. 4.26: Influence of the number of started photons N on the reconstruction. The standard detector configuration is used. For the number of photons, the IQR divided by N is given.

Background discrimination with hybrid scintillator

<div style="text-align: right">5</div>

NuDoubt^{++} utilizes a hybrid scintillator (as discussed in Section 3.1.2) offering the opportunity to discriminate background and signal events based on the ratio between scintillation and Cherenkov photons. This ratio differs for different particle types like electrons and positrons. For example, only positrons emit Cherenkov photons, not annihilation gammas, as Compton-scattered electrons' energies usually fall below the Cherenkov threshold. This leads to a higher C/s ratio for electrons compared to positrons.

In Section 5.1, the time resolution achievable in NuDoubt^{++} is discussed. The different amount of scintillation and Cherenkov light for various event categories is explained in Section 5.2. The results obtained from simulation is shown in Section 5.3, while in Section 5.4 the influence of the time resolution on the C/S ratio is examined. The last part, Section 5.5, focuses on the efficiency of event classification based on their C/S ratio.

Different strategies exist for separating Cherenkov and scintillation light signals in measurements. One approach involves examining different wavelength bands. Cherenkov light exhibits a broad spectrum, peaking in the UV region and falling off with λ^{-2} (as depicted in equation (3.5)), whereas scintillation light typically has a narrow spectrum. By selectively detecting long wavelength light, either through filters or red-sensitive photon detectors, it becomes feasible to capture Cherenkov photons without contamination from scintillation light. A crucial requirement for this method is that the scintillator emission spectrum remains minimal at long wavelength, ensuring that the Cherenkov light remains discernible. With this method, Cherenkov light can only be detected at longer wavelengths, making it challenging to utilize for events with minimal Cherenkov emission, as only a small fraction of the light is detectable. Previous studies have successfully identified Cherenkov light using LAB and PPO as scintillator [84]. Another approach is to separate fast Cherenkov light from slower scintillation light time-wise [85]. This can be achieved using slow scintillators in conjunction with fast photon detectors.

In principle, the required delay in scintillation times can be achieved by reducing the fluor concentration in the scintillator and thus the efficiency of the excitation transfer from solvent to fluor. However, this loss in efficiency is accompanied with a strong reduction in scintillation light yield. Another approach to achieve a slow organic scintillator is to mix two different solvents, as described in [86]. Those slow scintillators usually have time constants in the range of (10 to 30) ns, results in delayed scintillation light. This allows the early peak of Cherenkov light to be more visible. NuDoubt^{++} adopts this method, necessitating high time resolution to resolve the time difference.

5.1 Time resolution of the NuDoubt^{++} detector

The time resolution within a detector is influenced by various components. The determination of time resolution is simplified by combining theoretical distributions of individual components instead of directly including complex detector elements like OWL-fibers and SiPM readouts in the simulation. The distributions of the individual components are discussed in the following.

5.1.1 Light emission

The first contributor to time resolution is the emission of light. Cherenkov light, emitted promptly upon a particle traversing the scintillator, is assumed to follow a Delta distribution for emission time due to the negligible flight time of charged particles like electrons and positrons within the detector.

$$N_{\mathrm{C}}(t) = \delta(t) \, . \tag{5.1}$$

The time properties of the scintillator depend on its composition. For the NuDoubt^{++} experiment, the scintillator blend comprises 88 w.t % linear alkylbenzene (LAB) as solvent and 10 w.t. % Diisopropylnaphthalene (DIN) as co-solvent, and 2,5-Diphenyloxazole (PPO) at a concentration of 1 g/L as the fluor, with an additional 2 w.t. % of wax for opacity. This mixture is expected to yield approximately 9000 photons/ MeV. The time distribution of scintillators $N(t)_{\mathrm{Scint}}$ can be described by the exponential decay equation ((3.1)) for the de-excitation with the inclusion

Tab. 5.1: Scintillator emission timing parameters [86].

A_1	A_2	τ_r [ns]	τ_1 [ns]	τ_2 [ns]
0.44 ± 0.07	0.56 ± 0.07	1.20 ± 0.43	13.0 ± 3.4	26.3 ± 4.6
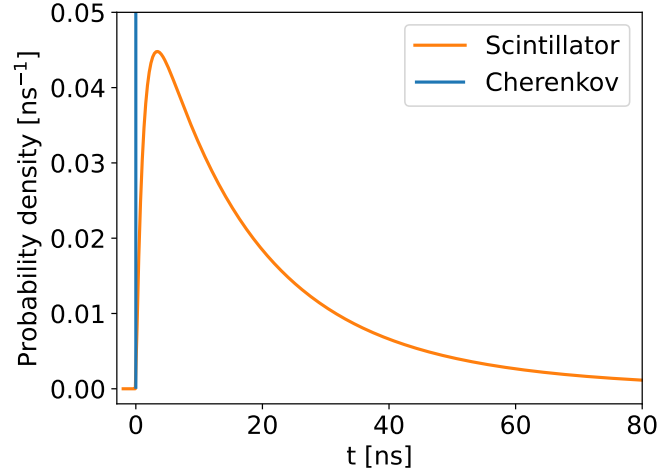
Fig. 5.1: Emission time spectra of Cherenkov and scintillation light.

of a rise time accounting for the excitation and energy transfer processes in the scintillator:

$$N_{\mathrm{S}}(t) = \sum_{i=1}^{2} A_i \frac{e^{t/\tau_i} - e^{t/\tau_r}}{\tau_i - \tau_r} \tag{5.2}$$

with

$$\sum_{i=1}^{2} A_i = 1 \, . \tag{5.3}$$

Here, τ_i represents the decay times for the prompt and delayed components, τ_r the scintillator rise time, and A_i denotes the normalization factors. For the scintillator devoid of wax, parameter values have been established previously [86], as listed in Table 5.1.

5.1.2 Propagation through the scintillator

The propagation of light through the opaque scintillator to fibers also contributes to the time resolution. Photons emitted within the scintillator encounter varying path lengths due to its high number of scatters, resulting in a spread of arrival
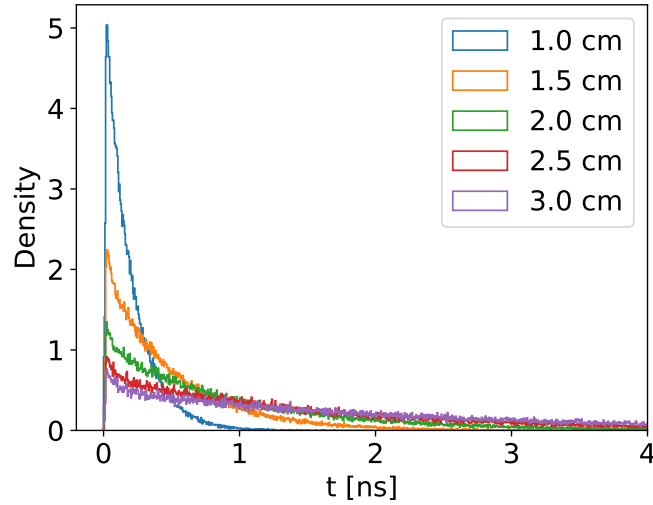
Fig. 5.2: Simulated time distribution of photons traveling through the scintillator to the OWL-fibers for different fiber spacing.

times at the OWL-fibers. The distribution also depends on the relative position from the photon start point to the fibers.

The dispersion is simulated by initiating 100 000 photons from different locations within the detector, corresponding to different distances from the fibers. The simulation results for the time until arriving at a fiber are illustrated in Figure 5.2. Approximately 90 % of the photons reach a fiber in less than 0.43 ns. The simulation employs fiber radii of 1.5 mm and a spacing of 10 mm. The scattering length was set to 1 mm, and the absorption length to 2 m. For comparison, the distribution was also simulated with larger fiber spacing. As expected, the distribution significantly widens. For 30 mm, 90 % of the photons now reach a fiber in under 5 ns.

5.1.3 OWL-fibers

In the case of OWL-fibers, the time distribution is a convolution of multiple effects: absorption and re-emission within the wavelength-shifting (WLS) paint, propagation through the fiber, and the detection time by the SiPM [87].
The SiPM is characterized by a Gaussian profile, conservatively assumed to have a a standard deviation of $\sigma_{\mathrm{SiPM}} = 0.1$ ns [62]. The wavelength-shifting mechanism follows an exponential decay, with the time constant determined by the specific composition of the wavelength shifter in use. Given the project's early stage, the

precise composition of the WLS paint is still work in progress. Consequently, the measured exponential decay time from the paint employed in the wavelength shifting optical module (WOM), recorded at $\tau_{\mathrm{WLS}} = 1.5\,\mathrm{ns}$ [59], serves as the basis for this analysis. An additional contribution stems from photon propagation within the fiber. After emission from the WLS paint, photon's emission angles determine whether they undergo total internal reflection or escape. For captured photons, the path length varies depending on the emission angle. The resultant path length distribution is approximated by an analytical model, called the flatten model, treating the fiber mantle as a flat rectangle [59]. This distribution, denoted as $N(d)$, is described by

$$N(d) = \frac{L}{d^2} \exp\left(-\frac{d}{\lambda_{\mathrm{att}}}\right) . \tag{5.4}$$

Here, L represents the fiber length, and λ_{att} denotes the attenuation length, including both scattering and absorption within the fiber. The propagation time distribution can be derived from $N(d)$ by substituting the path length d with time t multiplied with the photon velocity, given by the speed of light c divided by the refraction index n of the fiber medium:

$$N(t) = \frac{Ln^2}{c^2t^2} \exp\left(-\frac{ct}{n\lambda_{\mathrm{att}}}\right) . \tag{5.5}$$

The length of the fiber L is fixed to 1 m and for the attenuation length a value of 2 m is assumed. For quartz fibers the refraction index is 1.46.

The overall time distribution of the OWL-fiber emerges from the convolution of these three components, as depicted in Figure 5.3.

5.1.4 Overall time distribution

By convolving all the components (emission, propagation in scintillator, OWL-fiber), the overall time spread of the NuDoubt^{++} experiment can be derived.

$$N_{\mathrm{NuDoubt}}(t) = N_{\mathrm{Emission}}(t) * N_{\mathrm{Propagation}}(t) * N_{\mathrm{OWL-fiber}}(t) . \tag{5.6}$$

In Figure 5.4, the time distribution for different ratios of scintillation and Cherenkov light is depicted.

A distinct early peak in the combined distribution becomes evident when there is a relatively high proportion of Cherenkov light. Conversely, for a lower proportion
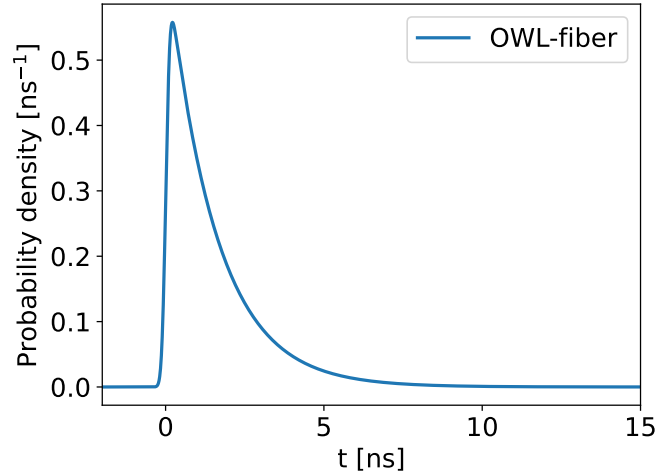
Fig. 5.3: Time distribution of the OWL-fiber, which is a convolution of the wavelength shifter, the propagation in the fiber and the detection in the SiPM.

of Cherenkov light, the peak is less pronounced and discernible. As the Cherenkov peak is visible, it suggests the potential for time-wise separation of Cherenkov and scintillation light using the slow scintillator employed in the NuDoubt^{++} experiment.

5.2 C/S ratio for different event categories

The hybrid scintillator technique is used to reduce background in the search for double beta decays. In this study, Geant4 simulations are used to quantify the production of scintillation (S) and Cherenkov (C) photons across various signal and background decay scenarios.

First, all double beta decay channels which can happen in NuDoubt^{++} are discussed, followed by the decays assumed to produce background in the detector.

5.2.1 Double beta decays

Four signal decays are targeted by NuDoubt^{++} : $2\nu\beta^+\beta^+$, $2\nu\text{EC}\beta^+$, and their respective neutrinoless counterparts. For this study the double beta isotope ^{78}Kr is used, which decays into ^{78}Se with a Q-value of $2.881\,\text{MeV}$. The C/S ratio differs for the decay channels as different amount of kinetic energy and number of ionizing

(a) S:C = 10:1 **(b)** S:C = 100:1
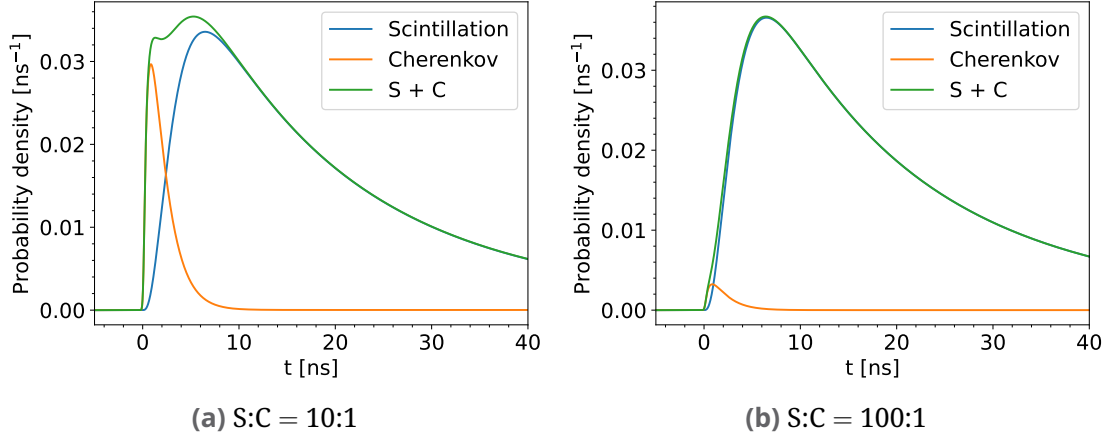
Fig. 5.4: The timing distribution of scintillation (S) and Cherenkov (C) light, as well as of the combined total light for two different ratios of their amount.

particles are released. In $\beta^+\beta^+$ decay, the total kinetic energy $T_{2\beta+}$ released is given by

$$T_{2\beta+} = Q - 4m_e \,, \tag{5.7}$$

while in ECβ^+ decay, it is higher due to only one positron annihilating:

$$T_{\mathrm{EC}\beta+} = Q - 2m_e - \epsilon_K \,. \tag{5.8}$$

Here, ϵ_K represents the K-shell electron binding energy, which for ^{78}Se equals 18 keV, resulting in $T_{2\beta+} = 837$ keV and $T_{\mathrm{EC}\beta+} = 1841$ keV for ^{78}Kr. m_e denotes the electron or positron mass, which lowers the kinetic energy of the positron if annihilation occurs.

The kinetic energy in two-neutrino modes is shared between positrons and neutrinos, leading to a continuous spectrum, whereas in the neutrinoless case, positron energy is discrete. Thus, the neutrinoless mode is always at the endpoint of the spectrum from the two-neutrino mode. The electron capture modes produce at least the amount of scintillation light corresponding to 1040 keV, the energy of two annihilation gammas plus the binding energy of the captured electron released as a de-excitation gamma ray. For double positron modes, the minimal scintillation light corresponds to 2044 keV, as four annihilation gammas are always produced. This minimum light output occurs when almost all kinetic energy is carried away by neutrinos rather than positrons. Electron capture modes also generate significantly more Cherenkov light. In these modes, the positron has more energy compared to the combined energy of two positrons in the double positron modes,

Tab. 5.2: Overview of signal and background decays. For all isotopes, the decay mode as well as the half-life is listed. Only the most probable decay channels with branching ratios higher than 90 % are listed. For the double beta decays, the expected half-life for the two-neutrino modes from theoretical models is given [88]. Energy refers to the endpoint energy for β decays and the discrete energy for α decays. All values are taken from [89].

Isotope	mode	daughter	$T_{1/2}$	energy [keV]
^{85}Kr	β^-	^{85}Rb	10.73 a	687.06
^{210}Bi	β^-	^{210}Po	5.01 d	1161.29
^{210}Po	α	^{206}Pb	138.38 d	5407.45
^{10}C	$\beta^+\gamma$	^{10}B	19.29 s	1903.02
^{11}C	β^+	^{11}B	20.33 min	960.21
^{78}Kr	$2\nu\beta^+\beta^+$	^{78}Se	$(4.94 - 15.8) \times 10^{25}$ a	837
^{78}Kr	$2\nu\mathrm{EC}\beta^+$	^{78}Se	$(1.34 - 4.41) \times 10^{22}$ a	1841

since only two annihilation gammas are produced instead of four. Positrons emit Cherenkov photons, whereas annihilation gammas do not, as Compton-scattered electrons have energies below the Cherenkov threshold. In the case of $0\nu\beta^+\beta^+$, the scintillation light is significantly lower compared to $0\nu\mathrm{EC}\beta^+$, despite both processes having the same total energy. This difference arises because the quenching effect is more pronounced for the two positrons in $0\nu\beta^+\beta^+$, resulting in a reduced amount of scintillation light.

5.2.2 Background events

There are various decays and interactions which are considered as background in the search for double beta decay. Background sources include the β^- decay of ^{85}Kr, with a relatively low Q-value of 687 keV but high decay rate due to its shorter half-life compared to the signal decays of ^{78}Kr. The abundance of this isotope is pretty low ($\sim 2 \times 10^{-11}$ [90]) and can be further decreased by the enrichment of ^{78}Kr.

Another source is ^{210}Bi, a typical background introduced during production of the scintillator, decaying via β^- decay into ^{210}Po with a Q-value of 1161 keV. The subsequent α decay into the stable ^{206}Pb produces minimal scintillation photons due to quenching and no Cherenkov light due to the high particle weight of α particles.

Moreover, background can arise from the electron recoil after scattering of solar neutrinos. Only the neutrinos from the ^{8}B decay in the sun has a high enough energy to fall within the energy range of the double beta decays. These neutrinos have a very low production rate in the sun and the reaction rate in the NuDoubt^{++} detector is small as the neutrino interaction cross section is low and the detection volume is small. This rare background is only relevant in the search for the rare neutrinoless modes. ^{85}Kr, ^{210}Bi and the solar neutrinos from ^{8}B all produce the same C/S signature in the detector because they all generate electrons. The only difference is that the energy spectrum of ^{85}Kr ends at lower energies than that of ^{210}Bi, while the maximum energy of neutrinos can exceed 10 MeV. An electron typically produces much more Cherenkov light than a positron for the same total visible energy (excluding neutrinos), as the kinetic energy of the electron is much higher. This is because the positron's energy is shared with two annihilation gammas. Consequently, backgrounds involving electrons can be distinguished from the double beta plus decay channels due to this difference in Cherenkov light output.

Moreover, gamma-ray background, primarily originating from radioactive contamination within the scintillator and OWL-fibers, pervades the whole energy spectrum interesting for NuDoubt^{++} (see Figure 5.5). These gamma rays emerge as a result of nuclear de-excitation subsequent to various decay processes. Gamma rays with energies over about 600 keV produce indirectly Cherenkov light, as then the energy of the Compton scattered electrons can exceed the Cherenkov threshold.

Additionally, spallation products from cosmic muons pose a significant challenge. This background is reducible by deep underground detector placement and coincidence veto with muon parent and spallation products like neutrons. However, the coincidence method is only effective for short-lived isotopes. Notably, ^{10}C and ^{11}C, created from carbon spallation, decay via β^+ decay into boron isotopes. Both isotopes fall within a similar energy range as the signal krypton decays. However, ^{10}C decay boasts a significantly shorter half-life compared to ^{11}C (c.f. Table 5.2). Consequently, ^{10}C is more readily reducible via the coincidence veto.

The decay of ^{11}C cannot be distinguished from the 2νECβ^+ decay based on event topology in the opaque scintillator since both decays emit positrons. The maximum kinetic energy of the positron is 0.960 MeV, overlapping with most of the energy spectrum of the 2νECβ^+ decay. Thus, discrimination using C/S ratio is not possible, as both decays result in the creation of one positron. The influence of the K-shell
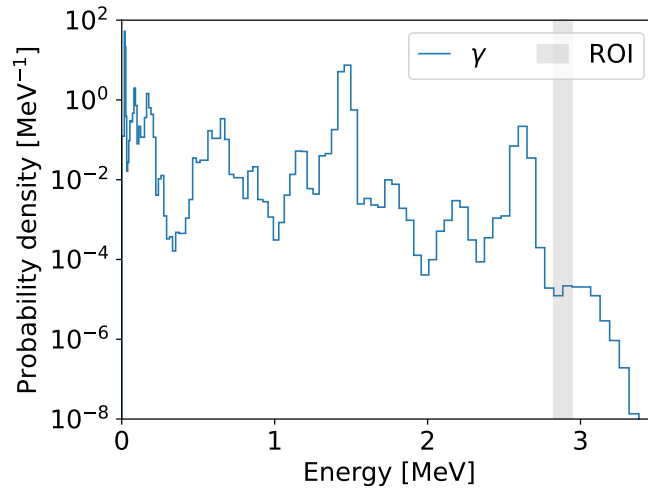
Fig. 5.5: Expected spectrum of the gamma ray background inside the detector. The ROI for the neutrinoless modes defined by the energy resolution is shown.

electron from the electron capture is minimal due to its low energy, leading to no difference in the C/S ratio between $2\nu EC\beta^+$ and ^{11}C.

The β^+ decay of ^{10}C occurs to an excited state of ^{10}B, resulting in the emission of an additional gamma ray from de-excitation. This provides an opportunity for event identification using both topology and the C/S ratio. With a branching ratio of 98.51 %, a gamma ray with 0.718 MeV is emitted. The positrons from this decay have an endpoint kinetic energy of 1.903 MeV. In the less common case (1.46 %), the gamma ray has a higher energy of 1.740 MeV, with the positron's maximum kinetic energy being 0.885 MeV. Due to the additional gamma, the β^+ decay of ^{10}C produces a minimum scintillation light amount corresponding to 1.740 MeV energy (de-excitation gamma plus two annihilation gammas), when all kinetic energy is carried away by the neutrino. For the same total energy without neutrinos, the ^{10}C has a lower C/S ratio compared to a single positron emission because the additional gamma produces Cherenkov light only when the energy of the Compton-scattered electrons is high. However, the ratio is still higher compared to double positron emission modes, due to the higher kinetic energy of the positron. Most of the time, there is a gamma with 0.718 MeV and two annihilation gammas, which is less than the energy of all four annihilation gammas in double positron events.
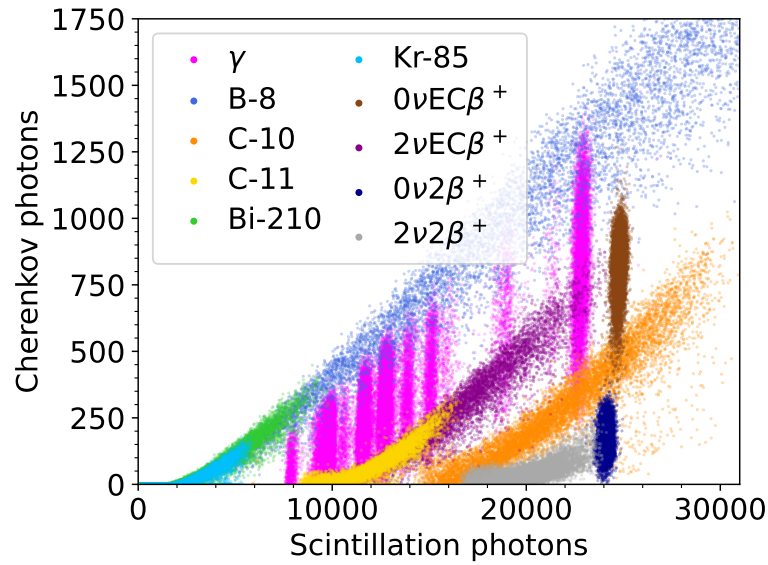
Fig. 5.6: Simulation of the amount of Cherenkov photons and scintillation photons created for several signal and background categories. 500 000 gammas were produced, for all other event categories 10 000 events each were simulated. A clear separation of the event categories is visible indicating that background discrimination with this method is possible.

5.3   Simulation results for C/S-ratio

In Figure 5.6, the number of created scintillation and Cherenkov photons in the simulation is illustrated for various decays. For the simulation of the double beta decays, the Geant4 extension *Bxdecay0* is used [70]. Notably, each event category comprises 10 000 simulated events, although these numbers do not reflect the actual expected rates in the detector, which can vary across different decay modes. Only for the gamma ray background 500 000 events were simulated with energies between 0.8 MeV and 2.9 MeV to incorporate the spectrum of them (see Figure 5.5). Omitted from the figure is the α-decay from ^{210}Po, as its Cherenkov component consistently remain near zero and thus is not visually discernible. The plot highlights the potential for discriminating between signal and background, evident by regions devoid of background events for each signal decay.

In a real detector, not all photons generated in the decay process are measured. For the NuDoubt^{++} detector, a predicted light yield of 800 PE/MeV (P.E = **P**hoton **E**quivalences) is assumed [44]. To account for this, the number of created photons is scaled down to this value and smeared with a Poisson distribution to incorporate
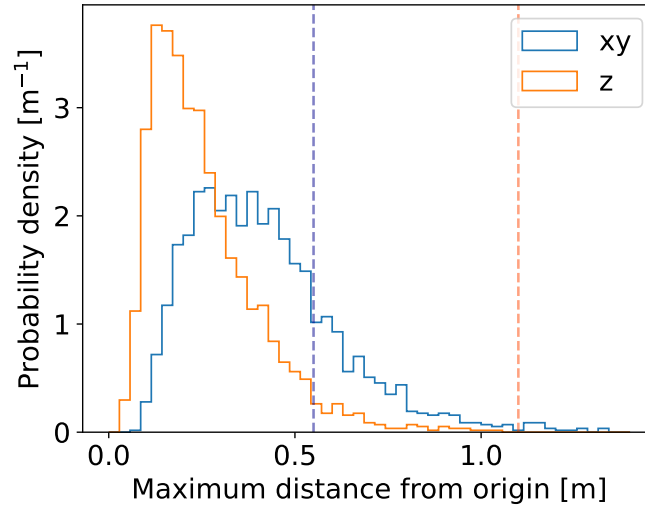
Fig. 5.7: Simulation of the event size of 511 keV annihilation gammas in the detector, when created in the middle (0,0,0). The maximum distance from the origin is given for the z-direction (parallel to the fibers) as well as in the x-y-plane. For both directions, the limit of the detector size is shown as vertical line.

the efficiency of the detection process. This leads to the event categories being less distinct.

However, it is important to note that in a real detector with a volume of approximately $1 \, \text{m}^3$, not all photons are contained within the detector volume. Gamma rays, due to their longer travel distances because of only small energy loss in Compton scattering processes, can traverse a significant path within the medium. In Figure 5.7, simulated annihilation gamma events ($E = 511 \, \text{keV}$) reveal the maximum distances in both the z-direction (parallel to the OWL-fibers) and the x-y-plane from the origin. While all simulated gamma events are contained within the 1.1 m detector length in the z-direction, only 79 % of the gammas are contained within the 0.55 m detector radius. Conversely, electrons and positrons, as well as α particles traverse much shorter paths within the detector ($\sim$ cm). Consequently, the scintillation and Cherenkov light emitted by these particles remain contained within the detector, barring events occurring really close to the detector limit.

Although there is a loss of scintillation light due to this effect, it is overlooked in this study as the energy, and thus the expected number of scintillation photons, can be reconstructed by considering only the first two Compton scatter blobs. Remarkably, in 99 % of events where gammas originate from the middle, these

two blobs are contained inside the detector volume.

By incorporating the OWL-fiber and SiPM efficiency (Figure 5.8), the distinc-
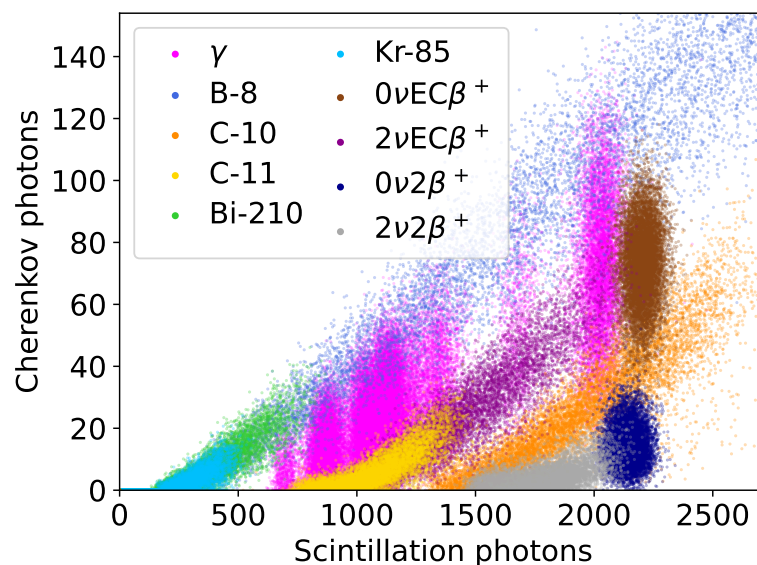
Fig. 5.8: Expected amount of measured photons for several signal and background categories, assuming a light yield of 800 PE/MeV. 500 000 gammas were produced, for all other event categories 10 000 events each were simulated.

tiveness of event categories diminishes compared to during their creation. Nevertheless, it appears feasible to identify events based on their Cherenkov and scintillation light levels. In this figure, also the importance of effectively reducing the presence of the two carbon isotopes for detecting the two-neutrino modes becomes clear, given their overlap with the signal in many parts.

5.4 Influence of time resolution on the C/S-ratio

As detailed in Section 5.1, the time resolution assumed for the NuDoubt^{++} detector enables the distinction of Cherenkov and scintillation photons within the measured light. However, due to the significant overlap in the time spectra of Cherenkov and scintillation light, their ratio can only be reconstructed with limited precision. Given a measured total number of photons, it is necessary to determine how accurately one can reconstruct the ratio of scintillation light to Cherenkov light.

The reconstruction performance is quantified using the Asimov approach, as explained in Section 4.6.3. Each data point in Figure 5.8 represents a measurement where the total number of measured photons is the sum of Cherenkov and scintillation light. The challenge is to reconstruct the C/S ratio, given that only the total number and the time distribution of photons are measured. Thus, the only fit parameter is the scintillation ratio r. The energy uncertainty is already applied in Figure 5.8.

The following function is fitted to the time distribution:

$$N(t, M|r) = (1 - r) \cdot M \cdot N_{\text{Cherenkov}}(t) + r \cdot M \cdot N_{\text{Scintillation}}(t), \qquad (5.9)$$

where r is the ratio of scintillation light in the total number of measured photons M. $N_{\text{Cherenkov}}(t)$ and $N_{\text{Scintillation}}(t)$ represent the normalized time distributions of Cherenkov and scintillation light in the detector (Equation 5.6). The optimal parameter is obtained by minimizing the χ^2 with respect to r:

$$\chi^2(r) = \sum_i \frac{(x_i - \mu_i)^2}{\sigma_i^2} = \sum_i \frac{(N(t_i, r_{\text{true}}) - N(t_i, r))^2}{\sigma_i^2}. \qquad (5.10)$$

Here, $N(t_i, r_{\text{true}})$ is the Asimov data set, constructed with the true parameter r_{true}. $N(t_i, r))$ is the distribution for different parameter values r, for which one wants to check the chi-squared value. For σ_i the Poisson uncertainty of $N(t_i, r))$ is taken: $\sigma_i = \sqrt{N(t_i, r))}$. The time distribution is binned in time with a bin size of 5 ps. Instead of fitting randomly generated pseudo-experiments, in the Asimov approach
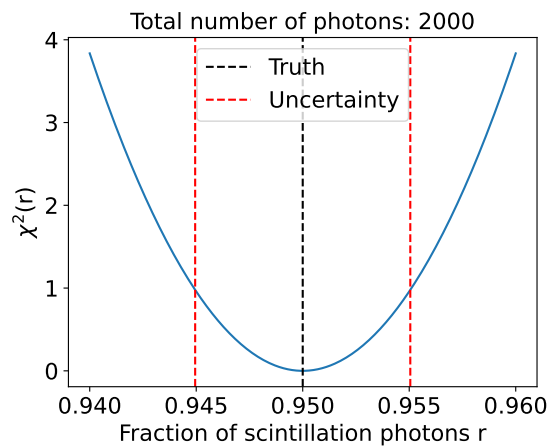
Fig. 5.9: χ^2 for different fraction of scintillation photons with a fixed total number of 2000 photons. In the Asimov approach, the minimum is at the true parameter.
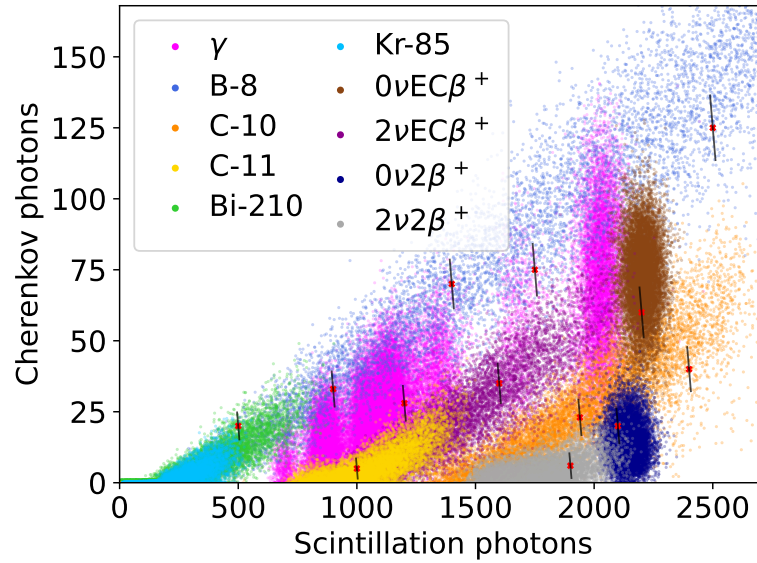
Fig. 5.10: Number of Cherenkov and scintillation photons from the reconstructed ratio. For some combinations of S and C, the 68 % confidence interval is shown with the black lines to get an estimate of the influence.

the exact model predictions are used. By construction, the minimum χ^2 is at the true value, with a χ^2 value of 0. The ratio where $\chi^2 = 1$ provides the 68 % confidence interval, which is used to estimate the uncertainty. In Figure 5.9 the shape of the χ^2 is shown for a fixed number of measured photons $M = 2000$ and a true ratio of $r = 0.95$. For this combination, the number of Cherenkov photons can be constrained within 10 % of the true value. This approach is applied to each data point in Figure 5.8. To obtain the reconstructed data, values are randomly sampled from a Gaussian distribution with the true ratio as mean and the 68 % confidence interval as standard deviation. This results in a slight smoothing of event categories, but the overall smearing is minimal due to the efficient C/S separation.

5.5 Event classification

The events are classified to the different event categories using a machine learning technique, explained in Section 5.5.1. Classification means, that for a measured number of Cherenkov and Scintillation one wants to predict with which probability

the event comes from which category. The performance of this classification is examined in Section 5.5.2.

5.5.1 Gradient Boosted Decision Trees

There are a lot of different machine learning techniques for classification tasks. One common method are Gradient Boosted Decision Trees (GBDT) [91]. They combine the strengths of decision trees with the boosting algorithm, resulting in an efficient method for predicting categorical outcomes. It combines the outputs of many smaller decision trees. The process starts with an initial prediction, then sequentially adds trees to correct the errors of previous predictions. By iteratively refining its predictions, GBDT produces a accurate final model.

In this analysis, the implementation from *Scikit-Learn* is used [92]. There are many options to optimize the training of the decision tree leading to better results. Here, no optimization is conducted, but rather the default options from the implementation are used. For each of the four signal events ($2\nu\beta^+\beta^+$, $2\nu\text{EC}\beta^+$, $0\nu\beta^+\beta^+$, $0\nu\text{EC}\beta^+$), a decision tree is trained using $2\,000\,000$ simulated gamma events and $100\,000$ each from the other categories. The signal always has the classifier 1 and all other events have the classifier 0.

5.5.2 Classification performance

The classification performance of the GBDT is evaluated using simulation data not included in the training set. Specifically, $750\,000$ gamma events and $100\,000$ events from each of the other categories are used for this evaluation. For each signal decay, a specific range of scintillation photons (and consequently energy) is defined for consideration, as events significantly outside the signal region are irrelevant and never classified as signal. Due to the quenching effect, the two neutrinoless modes have different ranges of scintillation photons. The cut values are determined by binning the energy with a bin size matching the energy resolution, and then converting this into the number of scintillation photons. For both neutrinoless modes, there were two bins containing almost all events, so these two bins were chosen. For the two-neutrino modes, the same upper bounds were applied, with the lower bound set at the first bin containing an event from this decay channel. For each simulated event, the GBDT outputs probabilities indicating

Tab. 5.3: Region of scintillation photons considered for the different decays.

Decay	Minimum	Maximum
$2\nu\beta^+\beta^+$	1422	2203
$2\nu\mathrm{EC}\beta^+$	731	2249
$0\nu\beta^+\beta^+$	2113	2203
$0\nu\mathrm{EC}\beta^+$	2158	2249

whether the event belongs to the signal or background. By applying thresholds based on these probabilities, a receiver operating characteristic (ROC) curve can be generated. In these ROC curves, the x-axis (logarithmic scale for improved visualization) represents the false positive rate (the fraction of background events incorrectly classified as signal), while the y-axis represents the true positive rate (signal efficiency, or the fraction of signal events correctly classified as signal). For comparison, 1:1 lines are also shown, representing the performance of a random classifier.

The ROC-curves for the four different signal event categories are shown in Figure 5.11. The classification performance for $2\nu\mathrm{EC}\beta^+$ and $0\nu\mathrm{EC}\beta^+$ is less effective, as indicated by their lower area under curve (AOC) values of 0.94 and 0.93, respectively. A perfect classifier would have a AUC of 1, so a higher AUC signifies a better classifier. High signal efficiencies in the EC channels lead to significantly higher background rates compared to double positron decays. This is expected because the C/S ratio of $2\nu\mathrm{EC}\beta^+$ completely overlaps with both the ^{11}C decay and the gamma background at low energies (see Figure 5.10). Additionally, $0\nu\mathrm{EC}\beta^+$ overlaps with the gamma ray background.

To determine the optimal cut probability for the signals, one must examine the sensitivity. The sensitivity for a signal with S events in the presence of B background events is given by:

$$\sigma = \frac{\epsilon_S S}{\sqrt{\epsilon_B B}} \, , \tag{5.11}$$

where ϵ_S is the signal efficiency (true positive rate) and ϵ_B is the false positive rate. Since the number of signal and background events (S and B) is independent from the cut value, maximizing the sensitivity involves finding the point on the ROC curve where

$$\frac{\epsilon_S}{\sqrt{\epsilon_B}} \tag{5.12}$$

is maximized. To account for the varying rates of different background event categories in the detector, the total false positive rate ϵ_B is calculated by summing

(a) $2\nu\beta^+\beta^+$

(b) $0\nu\beta^+\beta^+$

(c) $2\nu\mathrm{EC}\beta^+$

(d) $0\nu\mathrm{EC}\beta^+$
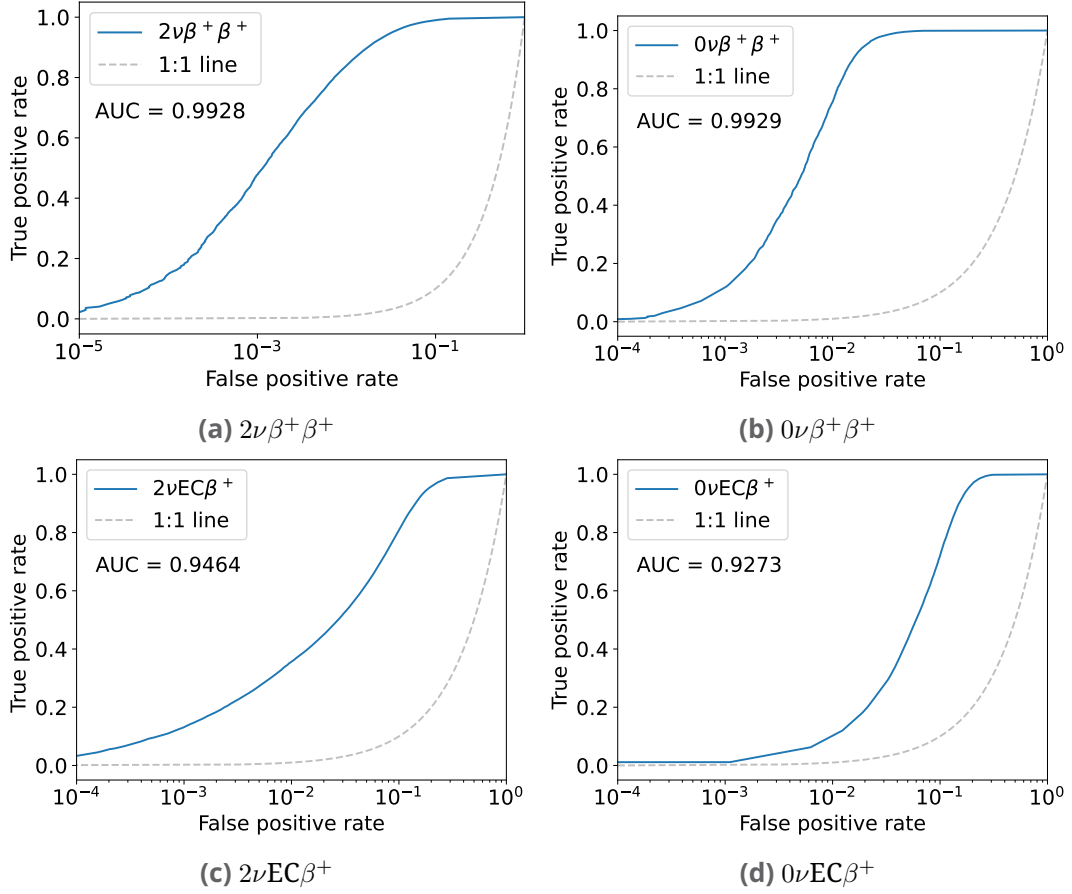
Fig. 5.11: ROC curves for the four signal event categories in the detector. The false positive rate is given in a logarithmic scale. For comparison, the 1:1 lines are shown in gray.

the false positive rates from all background contributions, each weighted by their expected rate R_i:

$$\epsilon_B = \sum_i \epsilon_{B,i} * R_i = \epsilon_{B,\gamma} * R_\gamma + \epsilon_{B,C-10} * R_{C-10} + \dots. \tag{5.13}$$

The sum of all R_i is normalized to one, as only the relative differences in occurrence of the categories is considered not their absolute values. This approach ensures that a background category with a high false positive rate but low relative occurrence is less impactful on sensitivity than one with a high rate in the detector. The rates are taken from [44, 93, 94].

The maximization is illustrated in Figure 5.12. As only the efficiency values are considered for finding the maximum and not the number of signal and background
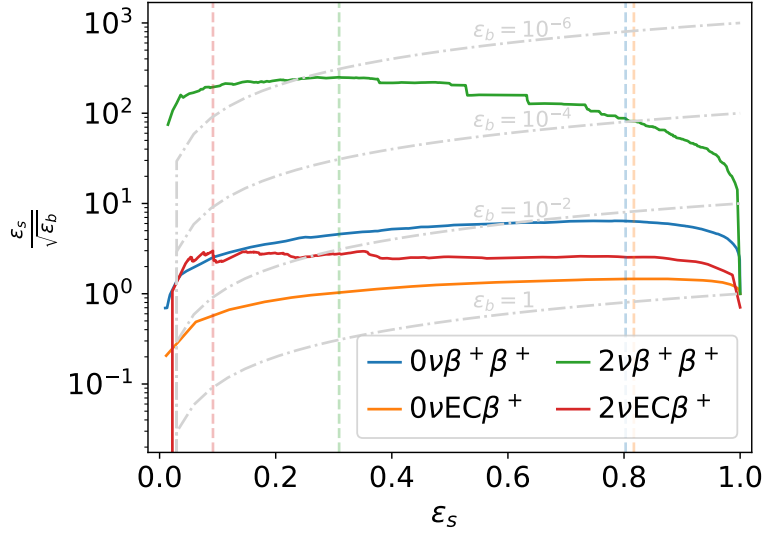
Fig. 5.12: The ratio of $\frac{\epsilon_S}{\sqrt{\epsilon_B}}$ as a function of signal efficiency. The maxima positions are indicated with vertical lines. Several lines of constant ϵ_B are shown in gray.

events, the absolute scale of the y-axis has no meaning for the actual sensitivity, which can be achieved. The optimal value for the two-neutrino modes are at lower signal efficiencies. For $2\nu EC\beta^+$, it is at a signal efficiency of only 9 %. For $2\nu\beta^+\beta^+$ it is higher, at 31 %. In contrast, for the neutrinoless modes, the optimal values are even higher, around 80 %.

In Figure 5.13, the false positive rate for each background source is plotted against the true positive rate for the different decays. The false positive rate for each background is calculated by dividing the number of events misclassified as signal by the total number of events in that background category. This provides an estimate of which backgrounds are most problematic. Additionally, the horizontal red line indicates the optimal signal efficiency calculated before.

The two-neutrino modes consistently contribute background to the neutrinoless modes and vice versa. However, because the predicted rates of neutrinoless modes are several orders of magnitude lower than those of two-neutrino modes, the background from neutrinoless decay in two-neutrino searches is negligible. In the neutrinoless double beta decay mode, the background rate from ^{10}C is approximately 4×10^{-2}, whereas for the electron capture case, it is slightly lower at 3×10^{-2}. The reduction of gamma ray background is highly effective in the double beta mode, achieving a rate as low as 7×10^{-4}. This contrasts with the neutrinoless

electron capture mode, where the gamma background rate is almost three orders of magnitude higher (52 %). For $0\nu\beta^+\beta^+$, in addition to the corresponding two-neutrino, there is a small contribution from the neutrinoless electron capture mode. In $0\nu EC\beta^+$, there is also background from solar neutrinos, but this can be lowered to a rate of 5×10^{-2} as the scattered electrons in the detector produce typically high amounts of Cherenkov light. For the $2\nu\beta^+\beta^+$ decay modes, the most significant background contribution comes from ^{11}C. Apart from this, the only other notable contribution is from the neutrinoless mode, indicating that this decay offers good opportunities for background discrimination, mainly because the gamma rays produce more Cherenkov light than the signal. In contrast, for the $2\nu EC\beta^+$ decay, achieving high signal efficiencies requires tolerating relatively high background rates due to significant overlap with gamma rays and ^{11}C. At the optimal cut value, which corresponds to a very low signal efficiency of just 9 %, the rates of background from both carbon isotopes and gamma rays are minimized to around 10^{-3}. While both neutrinoless modes also contribute to the background, their impact is negligible due to their low rates.

Overall, the main difference between the double beta mode and the electron capture mode is the much better gamma ray discrimination in the former, as these signals produce less Cherenkov light. It is evident that ^{10}C presents a significant background for all decay modes, emphasizing the importance of effective veto systems and substantial overburden for shielding. Furthermore, maintaining high radiopurity in the OWL-fibers and all materials used within the detector is crucial, as gamma ray background is particularly problematic in electron capture modes.

To determine the actual sensitivity of the experiment for the various double beta decay modes, it is necessary to consider the different expected event rates as well as the measurement run time. The signal rate also depends on how much krypton is loaded into the scintillator, which depends on the pressure during loading and the rate of isotope enrichment. In addition to using Cherenkov scintillation background discrimination, further discrimination based on the topology provided by the opaque scintillator is possible.

The simulation studies indicate that event classification using the C/S ratio, factoring in the time resolution of NuDoubt^{++} , is effective. However, there are significant differences in the performance across the double beta decay modes targeted by the detector. The $0\nu\beta^+\beta^+$ mode has demonstrated the greatest potential for background discrimination.
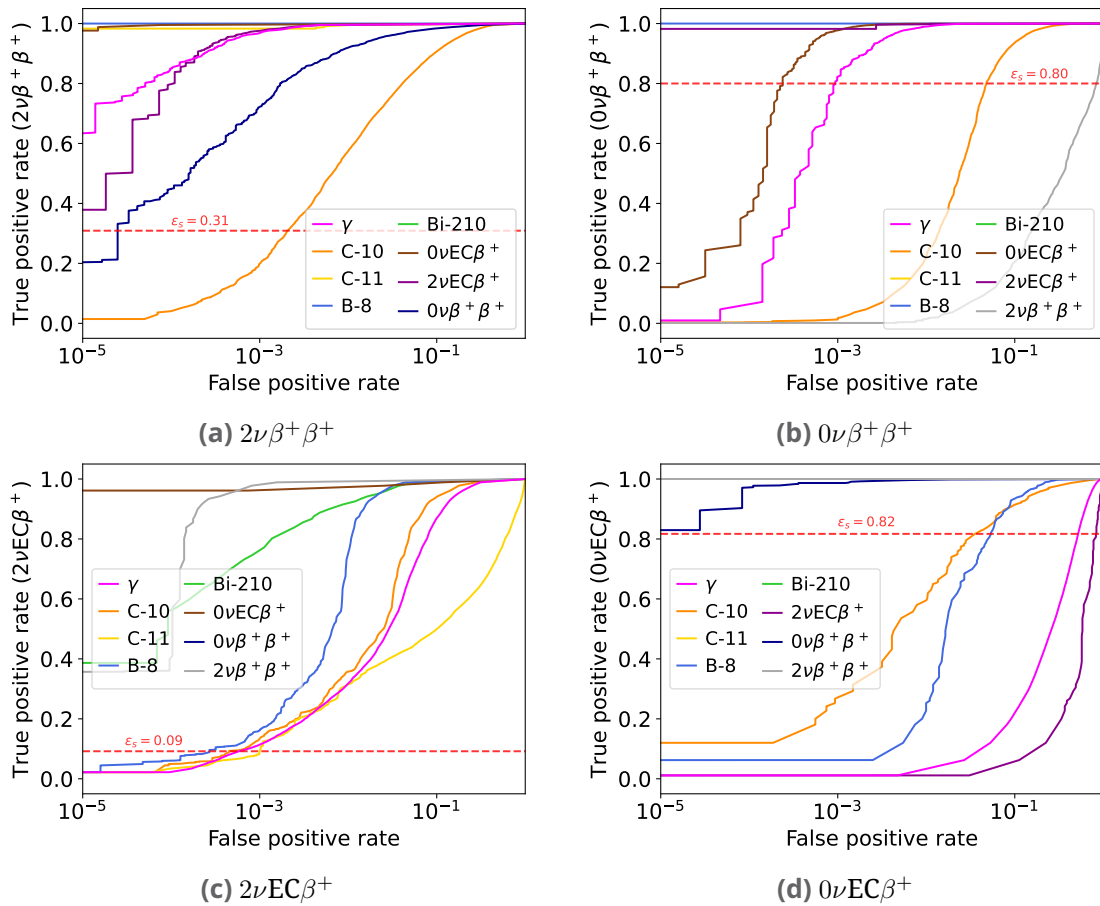
Fig. 5.13: False positive rates of the individual background sources depending on the signal efficiency.

Conclusion

In this thesis, a simulation of the NuDoubt^{++} detector was developed using the Geant4 simulation toolkit. This simulation offers the possibility to propagate particles through the opaque scintillator. The study primarily focused on the properties of the scintillator and the geometry of the detector, so spherical light sources were used as photon sources instead of directly simulating particles such as electrons or positrons. The processes of wavelength shifting within the OWL-fibers, photon propagation through the fibers, and detection by the SiPM were not simulated. This simplification was made because the OWL-fibers are still in development. Future work will include these processes in the simulation for more precise modeling of the detector. Nevertheless, the simplified version already provides a good opportunity to study the behavior in the opaque scintillator detector.

A position and energy reconstruction for photon bombs (photons starting from one point), based on likelihood using interpolation methods, was implemented. For a dense fiber grid, this reconstruction achieves a position resolution of 0.27 mm for 1 MeV photon bombs. The z-position, so the axis along which the fibers are aligned, is not reconstructed but can be included by taking the time difference between upper and lower SiPM of a fiber.

A photon number resolution of 4 % at 1 MeV is obtained. The resolution is defined as the 50 % interquartile range. The study demonstrated that the resolution significantly deteriorates with increased fiber spacing and larger scattering lengths. The absorption length as well as the fiber radius only have a minor influence in the investigated range. While the current interpolation-based reconstruction yields good results, further improvements may be possible by replacing the interpolation with e.g. a neural network.

In this thesis, photon bombs were simulated and reconstructed, where all photons originate from one point. Electrons or positrons rather leave a short track of several millimeters in the scintillator. Photons additionally produce several regions of scintillation light in the scintillator due to the Compton scattered electrons from the annihilation gammas. The reconstruction is not particularly suited for such

events, but can be expanded by allowing a short track in the reconstruction. For positrons and gammas, several photon bombs have to be considered.

Additionally, the potential for background discrimination using the hybrid scintillator was explored. The time resolution of the detector was approximated through theoretical assumptions and simulation results, indicating the capability to separate Cherenkov and scintillation light. Different background events for the double beta decays of ^{78}Kr were simulated. A Gradient Boosted Decision Tree (GBDT) classifier was used to test the background discrimination with the C/S ratio. Notably, for the neutrinoless double beta decay modes, significant discrimination was achieved for the double positron channel, reducing the high gamma ray background from radioactivity in the fibers and detector material by a factor of more than 1000. For the electron capture mode, the reduction is much smaller. Here, the factor is less than 2, suggesting that background discrimination in this case must rely heavily on topological discrimination which should be investigated in future studies. For all modes, efficient discrimination of the spallation-induced ^{10}C decay is accomplished.

Further improvement in background discrimination could be achieved by analyzing the Cherenkov to scintillation ratio for each fiber individually. The Cherenkov light distribution varies for different particles: positron events, which do not produce Cherenkov light via annihilation gammas, show Cherenkov light confined near the particle creation site (from the ionization tail of the positron itself). In contrast, higher energy gammas produce Cherenkov light at multiple locations due to Compton scattered electrons with high enough energy. Future research should investigate the combined discrimination potential of topology, the overall Cherenkov to scintillation ratio, and the ratio for each fiber individually to fully explore the capabilities of the NuDoubt^{++} experiment.

Bibliography

[1] J. D. Vergados, H. Ejiri, and F. Šimkovic. "Neutrinoless double beta decay and neutrino mass". In: *International Journal of Modern Physics E* 25.11 (Nov. 2016), p. 1630007 (cit. on p. 1).

[2] M. Agostini, G. R. Araujo, A. M. Bakalyarov, et al. "Final Results of GERDA on the Search for Neutrinoless Double-β Decay". In: *Phys. Rev. Lett.* 125 (25 Dec. 2020), p. 252502 (cit. on p. 1).

[3] E. Aprile, K. Abe, F. Agostini, et al. "Double-weak decays of ^{124}Xe and ^{136}Xe in the XENON1T and XENONnT experiments". In: *Phys. Rev. C* 106 (2 Aug. 2022), p. 024328 (cit. on pp. 1, 8).

[4] S. Abe, S. Asami, M. Eizuka, et al. "Search for the Majorana Nature of Neutrinos in the Inverted Mass Ordering Region with KamLAND-Zen". In: *Phys. Rev. Lett.* 130 (5 Jan. 2023), p. 051801 (cit. on p. 1).

[5] Wolfgang Pauli. "Pauli letter collection: letter to Lise Meitner". Typed copy (cit. on p. 3).

[6] Enrico Fermi. "Tentativo di una teoria dell'emissione dei raggi beta". In: *Ric. Sci.* 4 (1933), pp. 491–495 (cit. on p. 3).

[7] F. Reines and C. L. Cowan. "Detection of the Free Neutrino". In: *Phys. Rev.* 92 (3 Nov. 1953), pp. 830–831 (cit. on p. 3).

[8] G. Danby, J-M. Gaillard, K. Goulianos, et al. "Observation of High-Energy Neutrino Reactions and the Existence of Two Kinds of Neutrinos". In: *Phys. Rev. Lett.* 9 (1 July 1962), pp. 36–44 (cit. on p. 3).

[9] B. Adeva, O. Adriani, M. Aguilar-Benitez, et al. "A determination of the properties of the neutral intermediate vector boson Z0". In: *Physics Letters B* 231.4 (1989), pp. 509–518 (cit. on p. 3).

[10] P. Aarnio, P. Abreu, W. Adam, et al. "Measurement of the mass and width of the Z^0-particle from multihadronic final states produced in electron positron annihilations". In: *Physics Letters B* 231.4 (1989), pp. 539–547 (cit. on p. 3).

[11] D. Decamp, B. Deschizeaux, J.-P. Lees, et al. "A precise determination of the number of families with light neutrinos and of the Z boson partial widths". In: *Physics Letters B* 235.3 (1990), pp. 399–411 (cit. on p. 3).

[12] K. Kodama, N. Ushida, C. Andreopoulos, et al. "Observation of tau neutrino interactions". In: *Physics Letters B* 504.3 (Apr. 2001), pp. 218–224 (cit. on p. 3).

[13] MissMJ. *Standard Model of Elementary Particles*. Accessed: 2024-06-07. 2024 (cit. on p. 4).

[14] B. Pontecorvo. "Mesonium and anti-mesonium". In: *Sov. Phys. JETP* 6 (1957), p. 429 (cit. on p. 4).

[15] B. Pontecorvo. "Inverse beta processes and nonconservation of lepton charge". In: *Zh. Eksp. Teor. Fiz.* 34 (1957), p. 247 (cit. on p. 4).

[16] Ziro Maki, Masami Nakagawa, and Shoichi Sakata. "Remarks on the Unified Model of Elementary Particles". In: *Progress of Theoretical Physics* 28.5 (Nov. 1962), pp. 870–880 (cit. on p. 4).

[17] Raymond Davis, Don S. Harmer, and Kenneth C. Hoffman. "Search for Neutrinos from the Sun". In: *Phys. Rev. Lett.* 20 (21 May 1968), pp. 1205–1209 (cit. on p. 4).

[18] John N. Bahcall, M. H. Pinsonneault, and Sarbani Basu. "Solar Models: Current Epoch and Time Dependences, Neutrinos, and Helioseismological Properties". In: *The Astrophysical Journal* 555.2 (July 2001), pp. 990–1012 (cit. on p. 4).

[19] W. Hampel, J. Handt, G. Heusser, et al. "GALLEX solar neutrino observations: results for GALLEX IV". In: *Physics Letters B* 447.1 (1999), pp. 127–133 (cit. on p. 4).

[20] Bruce T. Cleveland, Timothy Daily, Jr. Raymond Davis, et al. "Measurement of the Solar Electron Neutrino Flux with the Homestake Chlorine Detector". In: *The Astrophysical Journal* 496.1 (Mar. 1998), p. 505 (cit. on p. 4).

[21] J. N. Abdurashitov, E. P. Veretenkin, V. M. Vermul, et al. "Solar neutrino flux measurements by the Soviet-American gallium experiment (SAGE) for half the 22-year solar cycle". In: *Journal of Experimental and Theoretical Physics* 95.2 (Aug. 2002), pp. 181–193 (cit. on p. 4).

[22] Y. Fukuda, T. Hayakawa, E. Ichihara, et al. "Measurement of the Solar Neutrino Energy Spectrum Using Neutrino-Electron Scattering". In: *Physical Review Letters* 82.12 (Mar. 1999), pp. 2430–2434 (cit. on p. 4).

[23] Y. Fukuda, T. Hayakawa, K. Inoue, et al. "Atmospheric ν_μ/ν_e ratio in the multi-GeV energy range". In: *Physics Letters B* 335.2 (1994), pp. 237–245 (cit. on p. 4).

[24] K.S. Hirata, T. Kajita, M. Koshiba, et al. "Experimental study of the atmospheric neutrino flux". In: *Physics Letters B* 205.2 (1988), pp. 416–420 (cit. on p. 4).

[25] M Ambrosio, R Antolini, C Aramo, et al. "Measurement of the atmospheric neutrino-induced upgoing muon flux using MACRO". In: *Physics Letters B* 434.3–4 (Aug. 1998), pp. 451–457 (cit. on p. 4).

[26] S. Ahlen, M. Ambrosio, R. Antolini, et al. "Atmospheric neutrino flux measurement using upgoing muons". In: *Physics Letters B* 357.3 (1995), pp. 481–486 (cit. on p. 4).

[27] Y. Fukuda, T. Hayakawa, E. Ichihara, et al. "Evidence for Oscillation of Atmospheric Neutrinos". In: *Physical Review Letters* 81.8 (Aug. 1998), pp. 1562–1567 (cit. on p. 4).

[28] Particle Data Group, R L Workman, V D Burkert, et al. "Review of Particle Physics". In: *Progress of Theoretical and Experimental Physics* 2022.8 (Aug. 2022), p. 083C01 (cit. on p. 5).

[29] M. Aker, A. Beglarian, J. Behrens, et al. "Direct neutrino-mass measurement with sub-electronvolt sensitivity". In: *Nature Physics* 18 (2 Feb. 2022), pp. 160–166 (cit. on p. 5).

[30] M. Goeppert-Mayer. "Double β-Disintegration". In: *Phys. Rev.* 48 (6 Sept. 1935), pp. 512–516 (cit. on p. 5).

[31] M. Alanssari, D. Frekers, T. Eronen, et al. "Single and Double β-Decay Q Values among the Triplet ^{96}Zr, ^{96}Nb, and ^{96}Mo". In: *Phys. Rev. Lett.* 116 (7 Feb. 2016), p. 072501 (cit. on p. 6).

[32] Matteo Agostini, Giovanni Benato, Jason A. Detwiler, Javier Menéndez, and Francesco Vissani. "Toward the discovery of matter creation with neutrinoless double beta decay". In: *Reviews of Modern Physics* 95.2 (May 2023) (cit. on pp. 6, 8, 20).

[33] Alexander Barabash. "Precise Half-Life Values for Two-Neutrino Double-beta Decay: 2020 Review". In: *Universe* 6.10 (2020) (cit. on p. 7).

[34] Magali Pujol, Bernard Marty, Pete Burnard, and Pascal Philippot. "Xenon in Archean barite: Weak decay of ^{130}Ba, mass-dependent isotopic fractionation and implication for barite formation". In: *Geochimica et Cosmochimica Acta* 73.22 (2009), pp. 6834–6846 (cit. on p. 8).

[35] Yu. M. Gavrilyuk, A. M. Gangapshev, V. V. Kazalov, et al. "Indications of $2\nu 2K$ capture in ^{78}Kr". In: *Phys. Rev. C* 87 (3 Mar. 2013), p. 035501 (cit. on p. 8).

[36] P. Belli, R. Bernabei, R.S. Boiko, et al. "First search for 2EC and ECβ processes in ^{168}Yb". In: *Nuclear Physics A* 990 (2019), pp. 64–78 (cit. on p. 8).

[37] M. Agostini, A. M. Bakalyarov, M. Balata, et al. "Probing Majorana neutrinos with double-beta decay". In: *Science* 365.6460 (2019), pp. 1445–1448 (cit. on p. 8).

[38] Luká š Gráf, Manfred Lindner, and Oliver Scholer. "Unraveling the neutrinoless double beta decay mechanisms". In: *Phys. Rev. D* 106 (3 Aug. 2022), p. 035022 (cit. on p. 8).

[39] J. Bernabeu, A. De Rujula, and C. Jarlskog. "Neutrinoless double electron capture as a tool to measure the electron neutrino mass". In: *Nuclear Physics B* 223.1 (1983), pp. 15–28 (cit. on p. 8).

[40] Jouni Suhonen. "Neutrinoless double beta decays of 106Cd revisited". In: *Physics Letters B* 701.4 (2011), pp. 490–495 (cit. on p. 8).

[41] Ronald Aylmer Fisher. "On the "Probable Error" of a Coefficient of Correlation Deduced from a Small Sample". en. In: *Metron* 1 (1921), pp. 3–32 (cit. on p. 9).

[42] R. A. Fisher. "Statistical Methods for Research Workers". In: *Breakthroughs in Statistics: Methodology and Distribution*. Ed. by Samuel Kotz and Norman L. Johnson. New York, NY: Springer New York, 1992, pp. 66–70 (cit. on p. 9).

[43] Allan Birnbaum. "On the Foundations of Statistical Inference". In: *Journal of the American Statistical Association* 57.298 (1962), pp. 269–306 (cit. on p. 10).

[44] M. Böhles, S. Böser, M. Eisenhuth, et al. *Combining Hybrid and Opaque Scintillator Techniques in Search for Double Beta Plus Decays: A Concept Study for the NuDoubt++ Experiment*. Work in progress (cit. on pp. 12, 19, 65, 72).

[45] J.B. BIRKS. "CHAPTER 8 - ORGANIC LIQUID SCINTILLATORS". In: *The Theory and Practice of Scintillation Counting*. Ed. by J.B. BIRKS. International Series of Monographs in Electronics and Instrumentation. Pergamon, 1964, pp. 269–320 (cit. on pp. 13, 14).

[46] T. Marrodán Undagoitia, F. von Feilitzsch, L. Oberauer, et al. "Fluorescence decay-time constants in organic liquid scintillators". In: *Review of Scientific Instruments* 80.4 (Apr. 2009) (cit. on p. 13).

[47] Paolo Lombardi, Fausto Ortica, Gioacchino Ranucci, and Aldo Romani. "Decay time and pulse shape discrimination of liquid scintillators based on novel solvents". In: *Nuclear Instruments and Methods in Physics Research Section A: Accelerators, Spectrometers, Detectors and Associated Equipment* 701 (2013), pp. 133–144 (cit. on p. 13).

[48] S. Gundacker, R.M. Turtos, E. Auffray, and P. Lecoq. "Precise rise and decay time measurements of inorganic scintillators by means of X-ray and 511 keV excitation". In: *Nuclear Instruments and Methods in Physics Research Section A: Accelerators, Spectrometers, Detectors and Associated Equipment* 891 (2018), pp. 42–52 (cit. on p. 13).

[49] "The Theory and Practice of Scintillation Counting". In: *Physics Today* 18.8 (1965), pp. 60–60 (cit. on p. 14).

[50] C Aberle, C Buck, F X Hartmann, S Schönert, and S Wagner. "Light output of Double Chooz scintillators for low energy electrons". In: *Journal of Instrumentation* 6.11 (Nov. 2011), P11006 (cit. on p. 14).

[51] Stefan Schoppmann. "Review of Novel Approaches to Organic Liquid Scintillators in Neutrino Physics". In: *Symmetry* 15.1 (2023), p. 11 (cit. on p. 14).

[52] Christian Buck, Benjamin Gramlich, and Stefan Schoppmann. "Novel Opaque Scintillator for Neutrino Detection". In: *JINST* 14.11 (2019), P11007. arXiv: 1908.03334 [physics.ins-det] (cit. on pp. 14, 21).

[53] A. Cabrera, A. Abusleme, J. dos Anjos, et al. "Neutrino physics with an opaque detector". In: *Communications Physics* 4.1 (Dec. 2021) (cit. on p. 15).

[54] P. A. Cherenkov. "Visible luminescence of pure liquids under the influence of γ-radiation". In: *Dokl. Akad. Nauk SSSR* 2.8 (1934), pp. 451–454 (cit. on p. 16).

[55] Thorsten Gluesenkamp. "On the Detection of Subrelativistic Magnetic Monopoles with the IceCube Neutrino Observatory". PhD thesis. Jan. 2010 (cit. on p. 16).

[56] I. M. Frank and I. E. Tamm. "Coherent visible radiation of fast electrons passing through matter". In: *Compt. Rend. Acad. Sci. URSS* 14.3 (1937), pp. 109–114 (cit. on p. 17).

[57] M. Askins et al. "THEIA: an advanced optical neutrino detector". In: *Eur. Phys. J. C* 80.5 (2020), p. 416 (cit. on p. 17).

[58] Steven D. Biller, Edward J. Leming, and Josephine L. Paton. "Slow fluors for effective separation of Cherenkov light in liquid scintillators". In: *Nuclear Instruments and Methods in Physics Research Section A: Accelerators, Spectrometers, Detectors and Associated Equipment* 972 (Aug. 2020), p. 164106 (cit. on p. 18).

[59] Benjamin Bastian-Querner, Lucas S. Binn, Sebastian Böser, et al. *The Wavelength-shifting Optical Module.* 2022. arXiv: `2112.12258 [astro-ph.IM]` (cit. on pp. 18, 31, 59).

[60] Kurtis F. Johnson. "Achieving the theoretical maximum light yield in scintillating fibers through non-uniform doping". In: *Nuclear Instruments and Methods in Physics Research Section A: Accelerators, Spectrometers, Detectors and Associated Equipment* 344.2 (1994), pp. 432–434 (cit. on p. 18).

[61] Bastian Keßler. "Development of Wavelength-shifting Fibers with high Photon Capture-Rate". MA thesis. Johannes Gutenberg University Mainz, 2024 (cit. on p. 18).

[62] Seul Ki Yang, J. Lee, Sug-Whan Kim, et al. "Precision measurement of the photon detection efficiency of silicon photomultipliers using two integrating spheres". In: *Opt. Express* 22.1 (Jan. 2014), pp. 716–726 (cit. on pp. 18, 58).

[63] C. Betancourt, A. Dätwyler, P. Owen, A. Puig, and N. Serra. "SiPM single photon time resolution measured via bi-luminescence". In: *Nuclear Instruments and Methods in Physics Research Section A: Accelerators, Spectrometers, Detectors and Associated Equipment* 958 (2020). Proceedings of the Vienna Conference on Instrumentation 2019, p. 162851 (cit. on p. 18).

[64] C. Saenz et al. "Results of a search for double positron decay and electron positron conversion of Kr-78". In: *Phys. Rev. C* 50 (1994), pp. 1170–1174 (cit. on p. 20).

[65] Pierluigi Belli, R. Bernabei, V.B. Brudanin, et al. "Search for Double Beta Decay of ^{106}Cd with an Enriched ^{106}CdWO$_4$ Crystal Scintillator in Coincidence with CdWO$_4$ Scintillation Counters". In: *Universe* 6.10 (Oct. 2020), p. 182 (cit. on p. 20).

[66] William Henry. "Experiments on the Quantity of Gases Absorbed by Water, at Different Temperatures, and under Different Pressures". In: *Philosophical Transactions of the Royal Society of London* 93 (1803), pp. 29–276 (cit. on p. 20).

[67] Lino Miramonti. "European underground laboratories: An overview". In: *AIP Conference Proceedings* 785.1 (Sept. 2005), pp. 3–11. arXiv: `0503054 [hep-ex]` (cit. on p. 21).

[68] M. Agostini et al. "Identification of the cosmogenic ^{11}C background in large volumes of liquid scintillators with Borexino". In: *Eur. Phys. J. C* 81.12 (2021), p. 1075. arXiv: `2106.10973 [physics.ins-det]` (cit. on p. 21).

[69] S. Agostinelli et al. "GEANT4–a simulation toolkit". In: *Nucl. Instrum. Meth. A* 506 (2003), pp. 250–303 (cit. on p. 23).

[70] F. Mauger and V. Tretyak. *BxDecay0, v1.1.1*. 2023 (cit. on pp. 24, 65).

[71] Karl Pearson. "The Problem of the Random Walk". In: *Nature* 72 (Aug. 1905) (cit. on pp. 24, 25).

[72] Lord Rayleigh. "XII. On the resultant of a large number of vibrations of the same pitch and of arbitrary phase". In: *The London, Edinburgh, and Dublin Philosophical Magazine and Journal of Science* 10.60 (1880), pp. 73–78 (cit. on pp. 24, 25).

[73] Mark Kac. "Random Walk and the Theory of Brownian Motion". In: *The American Mathematical Monthly* 54.7 (1947), pp. 369–391 (cit. on p. 25).

[74] Geoffroy Berthelot, Vincent Bansaye, and Sonia Said. *How to use random walks for modeling the movement of wild animals*. Mar. 2020 (cit. on p. 25).

[75] Eugene F. Fama. "Random Walks in Stock Market Prices". In: *Financial Analysts Journal* 21.5 (1965), pp. 55–59 (cit. on p. 25).

[76] Chris H. Rycroft and Martin Z. Bazant. *Introduction to Random Walks and Diffusion*. Lecture, Department of Mathematics, MIT. Feb. 2005 (cit. on p. 25).

[77] Christopher M Sorensen. "Rayleigh scattering". In: *Light Scattering and Absorption by Particles*. 2053-2563. IOP Publishing, 2022, 6-1 to 6–17 (cit. on p. 27).

[78] PhysicsOpenLab. *Light Scattering*. `https://physicsopenlab.org/2019/07/10/light-scattering/`. Accessed: 2024-06-10. 2019 (cit. on p. 28).

[79] "Radiative transfer. By S. Chandrasekhar. London (Oxford University Press) 1950. 8vo. Pp. 393, 35 figures. 35s". In: *Quarterly Journal of the Royal Meteorological Society* 76.330 (Oct. 1950), pp. 498–498 (cit. on p. 28).

[80] J. A. Nelder and R. Mead. "A Simplex Method for Function Minimization". In: *The Computer Journal* 7.4 (Jan. 1965), pp. 308–313 (cit. on p. 36).

[81] G.E. Fasshauer. *Meshfree Approximation Methods with MATLAB*. Interdisciplinary mathematical sciences. World Scientific, 2007 (cit. on p. 43).

[82] Glen Cowan, Kyle Cranmer, Eilam Gross, and Ofer Vitells. "Asymptotic formulae for likelihood-based tests of new physics". In: *The European Physical Journal C* 71.2 (Feb. 2011) (cit. on p. 49).

[83] William Howard Beasley and Joseph Lee Rodgers. "Bootstrapping and Monte Carlo Methods". In: *APA Handbook of Research Methods in Psychology, Vol. 2. Research Designs: Quantitative, Qualitative, Neuropsychological, and Biological*. Ed. by Harris Cooper, Paul M. Camic, Deborah L. Long, et al. American Psychological Association, 2012, pp. 407–425 (cit. on p. 52).

[84] T. Kaptanoglu, M. Luo, and J. Klein. "Cherenkov and scintillation light separation using wavelength in LAB based liquid scintillator". In: *Journal of Instrumentation* 14.05 (May 2019), T05001 (cit. on p. 55).

[85] C Aberle, A Elagin, H J Frisch, M Wetstein, and L Winslow. "Measuring directionality in double-beta decay and neutrino interactions with kiloton-scale scintillation detectors". In: *Journal of Instrumentation* 9.06 (June 2014), P06012 (cit. on p. 55).

[86] Hans Th. J. Steiger, Matthias Raphael Stock, Manuel Böhles, et al. *Development of a Bi-solvent Liquid Scintillator with Slow Light Emission.* 2024. arXiv: `2405.01100 [physics.ins-det]` (cit. on pp. 56, 57).

[87] Kyra Mossel. *Bachelorarbeit: Vertieftes Verständnis der Zeitantwort des Wellenlängen-schiebenden Optischen Modeuls (WOM).* 2022 (cit. on p. 58).

[88] Jouni Suhonen. "Analysis of double-β transitions in ^{78}Kr". In: *Phys. Rev. C* 87 (3 Mar. 2013), p. 034318 (cit. on p. 62).

[89] International Atomic Energy Agency - Nuclear Data Section. *Live Chart of Nuclides.* `https://www-nds.iaea.org/relnsd/vcharthtml/VChartHTML.html`. Apr. 2024 (cit. on p. 62).

[90] D.Yu. Akimov, A.I. Bolozdynya, A.A. Burenkov, et al. "New method of ^{85}Kr reduction in a noble gas based low-background detector". In: *Journal of Instrumentation* 12.04 (Apr. 2017), P04002–P04002 (cit. on p. 62).

[91] Jerome H. Friedman. "Greedy function approximation: A gradient boosting machine." In: *The Annals of Statistics* 29.5 (2001), pp. 1189–1232 (cit. on p. 70).

[92] *Scikit learn: GradientBoostingClassifier* (cit. on p. 70).

[93] Jouni Suhonen. "Analysis of double-β transitions in ^{78}Kr". In: *Phys. Rev. C* 87 (3 Mar. 2013), p. 034318 (cit. on p. 72).

[94] Magdalena Eisenhuth. Personal communication (cit. on p. 72).

List of Figures

List of Tables

Acknowledgement

First and foremost, I would like to thank Prof. Dr. Sebastian Böser for the great opportunity to work on this interesting project. My thanks go to the entire NuDoubt^{++} group, particularly Cloé Girard-Carillo and Veronika Palušová, for their patience in answering all my questions and their great support throughout this thesis. I am also grateful to the members of the AG Böser group for their support and the enjoyable lunch breaks that provided much-needed motivation and distraction. Special thanks to Jan Weldert for his countless hours of discussions and reviews. I am thankful to my family and friends, which were always a good help to come to other thoughts. Lastly, I want to thank Jimmy and Carlos, whose comforting presence made this thesis possible.